F. Setzwein, P. Ess, P. Gerlinger, An implicit high-order k-exact finite-volume approach on vertex-centered unstructured grids for incompressible flows, Journal of Computational Physics, Vol. 446 (2021), 110629

The original publication is available at www.elsevier.com

https://doi.org/10.1016/j.jcp.2021.110629

Preprint accepted in Journal of Computational Physics (originally submitted in December, 2020)
Link to journal version: https://doi.org/10.1016/j.jcp.2021.110629

An implicit high-order k-exact finite-volume approach on vertex-centered unstructured grids for incompressible flows

Florian Setzwein[a,*], Peter Ess[a,1], Peter Gerlinger[a,2]

[a]*German Aerospace Center (DLR), Institute of Combustion Technology, Stuttgart, 70569, Germany*

May 11, 2022

Abstract

We present a k-exact reconstruction method, which can be incorporated into vertex-centered unstructured finite-volume flow solvers to maintain a high-order accurate solution in space. The scheme is combined with a fractional step strategy for the solution of the incompressible Navier-Stokes equations with a fully implicit discretization of a Poisson equation for the pressure correction. This also involves a novel approach for the flux discretization in the k-exact framework. It is shown, that a third order of accuracy can be maintained for the discretization of convective fluxes and a second order of accuracy for diffusive fluxes, even on highly distorted grids. The scheme is implemented into ThetaCOM, a turbulent heat release extension of DLR's TAU code in its combustion version, showing its applicability to be used in a full production flow solver. The improved properties of our approach in terms of performance and accuracy are demonstrated with several benchmarks cases in both two and three spatial dimensions.

Keywords: High-Order Accuracy, k-Exact Reconstruction, Unstructured Grids, Finite-Volume Discretization, Projection Method, Incompressible Flow

1. Introduction

Unstructured high-order methods in Computational Fluid Dynamics are promised to reduce the computational effort for high-fidelity simulations employing complex geometries, due to enhanced resolution properties and a larger decrease of truncation errors [1, 2]. In the last decades various numerical tools have been developed for this task, such as the discontinuous Galerkin method [3, 4, 5, 6], the spectral volume method [7, 8, 9, 10] or spectral difference schemes [11, 12]. They all rely on the introduction of extra degrees of freedom within each computational cell. Thus, a higher order of accuracy is achieved, while information is only exchanged among face-neighboring elements. Such compact discretization approaches differ fundamentally in data structure and implementation from unstructured finite-volume schemes used in industrial production codes. Consequently, the integration of compact methods into established flow solvers requires a considerable effort for implementation, verification and validation [13].

However, several high-order discretization procedures for unstructured grids exist, which are based on the finite-volume method. These are essentially related to the k-exact reconstruction, which goes back to

*PhD Student, Corresponding author: Email: florian.setzwein@dlr.de;
[1]Postdoctoral fellow
[2]Professor

the work of Barth and Frederickson [14, 15] and which was further developed by Ollivier-Gooch et al. [16, 17, 18, 19]. Basically, the solution is locally reconstructed by means of piecewiese polynomials in every control volume, whose coefficients are typically estimated by means of least-squares approximations. Especially for compressible flows, the k-exact reconstruction is often combined with ENO/WENO approaches [20, 21, 22, 23] in order to stabilize the solution near discontinuities. All these methods are typically referred to as non-compact, since they involve a reconstruction over large stencils of elements. This is also their major drawback, since a large number of elements is required as the order of accuracy increases. As a consequence, the k-exact reconstruction on unstructured grids typically requires complex algorithms for the search and identification of element stencils [24, 25] and is prone to cache misses due to non-local data in memory [26] and the associated decrease in performance. Furthermore, the code scalability for parallel calculations is significantly affected [25, 27].

In recent years, several discretization techniques have been developed to overcome these difficulties. Haider et al. [27, 28, 29, 30] proposed an algorithm, where a k-exact reconstruction from non-local data is performed in an efficient way, that only involves exchange of data among adjacent cells. This is done by a recursive correction of the polynomial coefficients, which are related to approximate derivatives. These are determined by means of a least-squares approach, such that the reconstruction polynomials conserve the cell averages of all face-neighboring elements. Wang et al. [25, 26, 31] proposed the compact least-squares finite-volume method, which pursues a similar strategy as the procedure by Haider. Besides the conservation of cell averages, it further requires various orders of derivatives of dependent variables to conserve their means on face-neighboring elements. This leads to a system of linear equations that must be solved iteratively. Zhang et al. [32] introduced a multi-step reconstruction procedure where high-order accurate derivatives are estimated recursively by several least-squares relations to face-neighboring elements. Compared to Wang's compact least-squares method, this leads to an explicit reconstruction algorithm that features a higher efficiency for explicit schemes. A related strategy was emphasized in the multiple-correction method by Pont et al. [13, 33, 34] and recently by Menasria et al. [35], where the required derivative operators are computed with a Green-Gauss formulation. Compared to least-squares approaches, the latter should overcome problems that arise for highly stretched and irregular grids. The Green-Gauss derivatives are also corrected successively to higher levels of accuracy through several geometric correction matrices. All of the aforementioned approaches rely on a cell-centered grid structure. Recently, Bernard et al. [36] proposed an approach similar to the methods by Haider and Pont, which is intended for vertex-centered grids and which involves only one single correction step. It was shown, that the condition number of the resulting correction matrices is independent of the mesh size, in contrast to ordinary weighted least-squares approaches. However, their approach was only applied to the linear advection of a scalar quantity in the absence of boundary conditions.

To our knowledge, most k-exact reconstruction methods have been successfully applied to the simulation of compressible flows. Few attempts have been made to incorporate them for the solution of the time-dependent incompressible Navier-Stokes equations. These typically require advanced solution strategies, since the continuity equation is only present in terms of a constraint due to the vanishing temporal derivative of the density. Thus, it is not possible to rely on common temporal discretization schemes, which is typically done for purely hyperbolic systems of equations. Additionally, the pressure must be coupled to the velocity field in an adequate manner [37]. A common way to solve these problems are operator splitting techniques such as Chorin's projection method [38, 39]. Here, continuity is enforced through the solution of an equivalent substitute equation involving the Laplace operator [40]. The solution to the latter typically requires certain strategies to prevent the generation of spurious pressure oscillations [41]. This must be taken into account, if high-order methods are used for the solution process.

This paper is devoted to extending the multiple-correction method by Pont et al. [13] to vertex-centered unstructured grids, in order to achieve an enhanced numerical accuracy in space. A median-dual mesh representation is employed, which involves the storage of flow data at grid nodes and loops over grid edges for the calculation of numerical fluxes. It thus features less control-volumes and less flux-interfaces on most unstructured grids than a cell-centered approach [15]. Since the multiple-correction method requires the storage of grid dependent tensor metrics at exactly these entities, a vertex-centered representation significantly reduces the memory requirements. The proposed scheme is incorporated into a fractional

step strategy for the solution of the incompressible Navier-Stokes equations, where a fully implicit Poisson equation for the pressure is solved. The solution procedure for the latter is slightly modified, such that it does not require the usage of auxiliary stabilization terms to prevent spurious pressure oscillations. Besides this, a novel discretization of convective and diffusive fluxes in the k-exact framework is presented. Even on highly irregular meshes, it maintains a third order accurate convective and a second order accurate diffusive transport in space. It will be shown, that our scheme can be used in full production finite-volume flow solvers for unstructured grids. For this purpose it is implemented in DLR's ThetaCOM code (**t**urbulent **he**at release extension for **TA**U in its **com**bustion version) [42, 43, 44, 45, 46, 47, 48, 49], which features a memory-efficient matrix free Krylov solver for the system of linear equations and multigrid preconditioning for the Poisson equation. The 1- and 2-exact projection method and corresponding flux discretization methods are examined by means of several canonical test cases in $2D$. Further benchmarks are carried out to demonstrate the enhanced spatial accuracy properties for the simulation of incompressible laminar flows in two and three dimensions on fully unstructured grids and in the presence of boundary conditions. The overall performance gain of this high-order approach is assessed by comparison of all benchmark results with conventional spatial discretization schemes.

2. Fundamentals of the k-exact multiple-correction method

This section gives a brief introduction to the k-exact finite-volume discretization. It will then be shown how the multiple-correction approach by Pont et al. [13] can be extended to vertex-centered grids. In addition, the corresponding correction matrices for the cases $k = 1$ and $k = 2$ will be derived. As a starting point, consider a general transport equation, which describes the convection and the diffusion of any scalar quantity ϕ in a flow field with velocity $\mathbf{u}$ and diffusivity D

$$\frac{\partial \phi}{\partial t} + \frac{\partial}{\partial x_i}\left(u_i \phi\right) + \frac{\partial}{\partial x_i}\left(D \frac{\partial \phi}{\partial x_i}\right) = S. \tag{1}$$

The term S incorporates local sources and sinks of ϕ. For simplification, the diffusivity D is assumed to be constant in space and independent of the local concentration of the scalar. Equation (1) is solved in a domain $\Omega \subset \mathbb{R}^d$, which is discretized by a set of linear elements, referred to as the primary grid $\mathcal{P}(\Omega)$. It consists of tetrahedra, hexahedra, prisms or pyramids for $d = 3$ or triangles and quadrilaterals for $d = 2$. The edge-based representation of $\mathcal{P}(\Omega)$ is obtained by constructing polyhedrons from the centroids of adjacent elements, faces and edges around each primary grid node. This representation is referred to as median-dual grid $\mathcal{D}(\Omega)$ and it consists of N non-overlapping complex polyhedral elements Ω_α that are compounds of triangular faces [50]. Two elements Ω_α and Ω_β are called adjacent, if they share a common face $A_{\alpha\beta}$. All adjacent elements of a cell Ω_α are referred to as its 1^{st} neighborhood, signed as $\mathbb{V}_\alpha^{(1)}$. The n^{th} neighborhood of Ω_α is defined recursively with the neighborhoods of its adjacent elements $\mathbb{V}_\alpha^{(n)} := \bigcup_{\gamma \in \mathbb{V}_\alpha^{(n-1)}} \mathbb{V}_\gamma^{(1)}$. Figure 1 shows a primary grid $\mathcal{P}(\Omega)$, its respective median-dual tessellation $\mathcal{D}(\Omega)$ and the first and second neighborhood of a median-dual cell Ω_α for $d = 2$.

Fundamental to the k-exact finite-volume discretization is the volume-average $\overline{\phi}_\alpha$ of an element Ω_α

$$\overline{\phi}_\alpha = \frac{1}{|\Omega_\alpha|} \iiint_{\Omega_\alpha} \phi(\mathbf{x}) \, \mathrm{d}V, \tag{2}$$

where $|\Omega_\alpha|$ denotes the volume of the element. In the proposed method, the volume-average $\overline{\phi}_\alpha$ of an element Ω_α is stored at its respective primary grid node $\mathbf{x}_\alpha$. Note that this is a major difference to the node-centered edge-based method that is popular for compressible flow problems, where a point-valued solution is stored at these locations instead [51, 52, 53, 54, 55]. In the scope of a Godunov scheme, the volume-averaging is applied to equation (1) such that the averages $\overline{\phi}_\alpha$ act as degrees of freedom. This leads

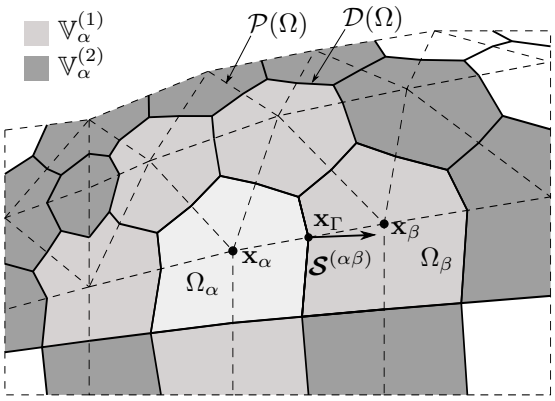

Figure 1: Median-dual grid in 2D, indicated in solid lines. The corresponding primary grid is drawn in dashed lines. The simulation variables are stored at the location of primary grid nodes, e.g. $\mathbf{x}_\alpha$ or $\mathbf{x}_\beta$.

to the following system of N equations:

$$\frac{\partial \overline{\phi}_\alpha}{\partial t} + \frac{1}{|\Omega_\alpha|} \sum_{\beta \in \mathbb{V}_\alpha^{(1)}} \left[\iint_{A_{\alpha\beta}} (u_i \phi)\, n_i \,\mathrm{d}A + \iint_{A_{\alpha\beta}} \left(D \frac{\partial \phi}{\partial x_i} \right) n_i \,\mathrm{d}A \right] = \overline{S}_\alpha. \tag{3}$$

The surface integrals are referred to as fluxes and must be approximated in order to close the system of equations. To solve equation (3) using the k-exact reconstruction approach, essentially three steps are required [15]:

1. Reconstruct the solution of the primitive field variables from known volume-averages in the vicinity of Ω_α at a time step t_n
2. Approximate the fluxes at element interfaces with a higher order of accuracy using the reconstructed solution of the adjacent elements.
3. Let the system of equations evolve in time to estimate new volume-averages at a new time step t_{n+1}.

The reconstruction for an element Ω_α is carried out through a polynomial function of degree k, denoted by $\phi^{(k+1)}(\mathbf{x}; \mathbf{x}_\alpha)$, which must satisfy the k-exactness constraint [15]

$$\phi^{(k+1)}(\mathbf{x}; \mathbf{x}_\alpha) = \phi(\mathbf{x}) + \mathcal{O}\left(h^{k+1}\right), \tag{4}$$

with h being a characteristic width of the element and $\phi(\mathbf{x})$ the exact value of ϕ at location $\mathbf{x}$. The superscript in brackets indicates the order of accuracy to approximate the solution. To estimate the unknown polynomial coefficients, at least $\binom{k+d}{k}$ averages $\overline{\phi}$ must be provided [27]. This set of associated elements will be denoted by $\mathcal{N}_\alpha$ and it is required that all these elements are located in the vicinity of Ω_α. Typically, a larger number of elements is used in order to stabilize the reconstruction. A requirement for $\phi^{(k+1)}(\mathbf{x}; \mathbf{x}_\alpha)$ is the conservation of the mean, which states that the reconstruction polynomial must preserve the volume-average of ϕ on Ω_α with an appropriate order of accuracy. Furthermore, the volume-averages $\overline{\phi}_\beta$ of all cells in the support $\mathcal{N}_\alpha$ must be conserved as well

$$\frac{1}{|\Omega_\alpha|} \iiint_{\Omega_\alpha} \phi^{(k+1)}(\mathbf{x}; \mathbf{x}_\alpha)\,\mathrm{d}V = \overline{\phi}_\alpha + \mathcal{O}\left(h^{k+1}\right), \tag{5a}$$

$$\frac{1}{|\Omega_\beta|} \iiint_{\Omega_\beta} \phi^{(k+1)}(\mathbf{x}; \mathbf{x}_\alpha)\,\mathrm{d}V = \overline{\phi}_\beta + \mathcal{O}\left(h^{k+1}\right), \qquad \forall \beta \in \mathcal{N}_\alpha. \tag{5b}$$

The reconstruction function of a median-dual cell Ω_α can be expressed by means of a Taylor-polynomial of

degree k

$$\phi^{(k+1)}(\mathbf{x};\mathbf{x}_\alpha) = \phi\Big|_{\mathbf{x}_\alpha}^{(k+1)} + \frac{\partial\phi}{\partial x_{i_1}}\Big|_{\mathbf{x}_\alpha}^{(k)} (x_{i_1} - x_{i_1,\alpha}) + \ldots + \frac{1}{k!}\frac{\partial^k\phi}{\partial x_{i_1}\ldots\partial x_{i_k}}\Big|_{\mathbf{x}_\alpha}^{(1)} (x_{i_1} - x_{i_1,\alpha})\ldots(x_{i_k} - x_{i_k,\alpha})\,. \quad (6)$$

The point of evaluation $\mathbf{x}_\alpha$ is the primary grid position, around which Ω_α is constructed and $\phi|_{\mathbf{x}_\alpha}^{(k+1)}$ refers to the approximation of the point value $\phi(\mathbf{x}_\alpha)$ with an accuracy of $\mathcal{O}(h^{k+1})$. Respectively, the derivative terms denote k-exact differentiation operators, which approximate the n^{th} derivative of ϕ at $\mathbf{x}_\alpha$ with an accuracy of $\mathcal{O}(h^{k-n+1})$. The point value $\phi|_{\mathbf{x}_\alpha}^{(k+1)}$ can be related to the volume-average $\overline{\phi}_\alpha$ by applying operator (2) on the reconstruction polynomial (6)

$$\phi\Big|_{\mathbf{x}_\alpha}^{(k+1)} = \overline{\phi}_\alpha - \frac{\partial\phi}{\partial x_{i_1}}\Big|_{\mathbf{x}_\alpha}^{(k)} \mathcal{M}_{i_1}^{(\alpha,\alpha)} - \ldots - \frac{1}{k!}\frac{\partial^k\phi}{\partial x_{i_1}\ldots\partial x_{i_k}}\Big|_{\mathbf{x}_\alpha}^{(1)} \mathcal{M}_{i_1\ldots i_k}^{(\alpha,\alpha)} + \mathcal{O}\left(h^{k+1}\right). \quad (7)$$

Equation (7) can thus be used to determine $\phi|_{\mathbf{x}_\alpha}^{(k+1)}$ in the reconstruction polynomial with an appropriate accuracy, if the corresponding derivatives at $\mathbf{x}_\alpha$ are known. The terms $\mathcal{M}_{i_1\ldots i_p}^{(\alpha,\alpha)}$ are referred to as rank p geometric volume moment tensors. These quantities are of major importance to maintain a higher order of accuracy, especially on highly distorted grids. They are defined in a general way for a volume Ω_β and any point $\mathbf{x}_\alpha$ by

$$\mathcal{M}_{i_1 i_2\ldots i_p}^{(\beta,\alpha)} = \frac{1}{|\Omega_\beta|}\iiint_{\Omega_\beta} (x_{i_1} - x_{i_1,\alpha})\,(x_{i_2} - x_{i_2,\alpha})\ldots\left(x_{i_p} - x_{i_p,\alpha}\right)\,\mathrm{d}V \quad (8)$$

and can be calculated analytically prior to the simulation. The first superscript β denotes the volume Ω_β for performing the averaging and the second superscript α denotes the point $\mathbf{x}_\alpha$ used for centering the moment. For a detailed explanation and formulas on the calculation of geometric moment tensors for polyhedral elements we refer to the literature [56, 57]. The rank one volume moment tensor $\mathcal{M}_i^{(\alpha,\alpha)}$ simply expresses the distance of a primary grid node $\mathbf{x}_\alpha$ towards the geometric centroid of the median-dual element Ω_α. It reduces to zero if both coincide. On the contrary, the symmetric rank two volume moment tensors $\mathcal{M}_{ij}^{(\alpha,\alpha)}$ eigenvalues describe the moments of inertia of Ω_α towards $\mathbf{x}_\alpha$ and it does not equal zero [36]. The proposed method requires geometric moments $\mathcal{M}_{i_1 i_2\ldots i_p}^{(\beta,\alpha)}$ between two adjacent cells Ω_α and Ω_β. However, only the moment tensors $\mathcal{M}_{i_1 i_2\ldots i_p}^{(\alpha,\alpha)}$ must be stored for each element, since $\mathcal{M}_{i_1 i_2\ldots i_p}^{(\beta,\alpha)}$ can be deduced from binomial expansion [17, 58]. The following relations can be obtained for the rank one and rank two volume moments:

$$\mathcal{M}_i^{(\beta,\alpha)} = \mathcal{M}_i^{(\beta,\,\beta)} + (x_{i,\,\beta} - x_{i,\alpha})\,, \quad (9a)$$

$$\mathcal{M}_{ij}^{(\beta,\alpha)} = \mathcal{M}_{ij}^{(\beta,\,\beta)} + (x_{i,\,\beta} - x_{i,\alpha})\,\mathcal{M}_j^{(\beta,\,\beta)} + (x_{j,\,\beta} - x_{j,\alpha})\,\mathcal{M}_i^{(\beta,\,\beta)} + (x_{i,\,\beta} - x_{i,\alpha})\,(x_{j,\,\beta} - x_{j,\alpha})\,. \quad (9b)$$

It remains to approximate the unknown derivative operators in Equations (6) and (7) with appropriate accuracies. This is often addressed with a least-squares approach over all elements in the stencil $\mathcal{N}_\alpha$. But especially for $d = 3$, a high number of elements is required to ensure a stable reconstruction. A further problem is that most elements in $\mathcal{N}_\alpha$ are not adjacent to Ω_α. To exchange information among $\mathcal{N}_\alpha$, complex data structures are required which leads to performance implications in terms of cache misses due to non-local memory access [26, 27]. Furthermore, if the entire domain Ω is decomposed for parallel computations, data packages of stencils that are distributed among domains must be exchanged. Since these overlapping stencils may vary in size, this also applies to the resulting data packages, which limits the parallel efficiency of the code [25, 27].

These problems are avoided in the multiple-correction approach, where the unknown derivatives are determined through approximate Green-Gauss gradients, that only involve exchange of information between

face-neighboring elements. Since these *a priori* derivatives do not meet the required k-exactness constraints, they must be corrected with certain matrices, which successively increase their k-exactness level. These correction matrices depend solely on the mesh geometry and are calculated prior to the simulation, if the grid-structure is not varying in time. In the following sections, the correction matrices needed for 1- and 2-exact derivatives on vertex-centered grids will be derived.

2.1. 1*-exact reconstruction*

As a starting point, the gradient of the solution must be somehow approximated from available volume-averages from face-neighboring elements of Ω_α. This is done with a Green-Gauss gradient operator, which is widely used in vertex-centered codes [59]

$$\left.\frac{\partial \phi}{\partial x_i}\right|_{\mathbf{x}_\alpha}^{(0)} := \frac{1}{|\Omega_\alpha|} \sum_{\beta \in \mathbb{V}_\alpha^{(1)}} \frac{1}{2} \left(\overline{\phi}_\alpha + \overline{\phi}_\beta\right) \mathcal{S}_i^{(\alpha\beta)}. \tag{10}$$

Here, $\boldsymbol{\mathcal{S}}^{(\alpha\beta)}$ refers to the joint normal of all sub-faces of the median-dual face $A_{\alpha\beta}$. Its norm equals the surface area $|A_{\alpha\beta}|$. As already mentioned, the superscripts of point values enclosed in brackets serve to emphasize the order of accuracy. Thus, the gradient operator in equation (10) features a discretization error of $\mathcal{O}(1)$. As it will shown below, this error occurs if the grid is deformed to a certain degree. To deduce a 1-exact gradient operator, the solution of $\phi(\mathbf{x})$ is approximated through a Taylor series expansion of degree one

$$\phi(\mathbf{x}) = \phi\Big|_{\mathbf{x}_\alpha} + \left.\frac{\partial \phi}{\partial x_i}\right|_{\mathbf{x}_\alpha} (x_i - x_{i,\alpha}) + \mathcal{O}\left(h^2\right). \tag{11}$$

Note that these point values without superscripts refer to the actual solution and its derivatives at the position $\mathbf{x}_\alpha$. To relate the available volume-averages to this Taylor polynomial, equation (11) is volume-averaged over element Ω_α and all elements in its first neighborhood $\mathbb{V}_\alpha^{(1)}$. The following equations result under consideration of the geometric volume moment tensor definition in equation (8)

$$\overline{\phi}_\alpha = \phi\Big|_{\mathbf{x}_\alpha} + \left.\frac{\partial \phi}{\partial x_i}\right|_{\mathbf{x}_\alpha} \mathcal{M}_i^{(\alpha,\alpha)} + \mathcal{O}\left(h^2\right), \tag{12}$$

$$\overline{\phi}_\beta = \phi\Big|_{\mathbf{x}_\alpha} + \left.\frac{\partial \phi}{\partial x_i}\right|_{\mathbf{x}_\alpha} \mathcal{M}_i^{(\beta,\alpha)} + \mathcal{O}\left(h^2\right) \tag{13}$$

These expressions for the averages $\overline{\phi}_\alpha$ and $\overline{\phi}_\beta$ are inserted into the Green-Gauss gradient operator (10) for which the geometric conservation property is exploited

$$\sum_{\beta \in \mathbb{V}_\alpha^{(1)}} \mathcal{S}_i^{(\alpha\beta)} = 0. \tag{14}$$

It is now possible to relate the gradient operator (10) to the actual derivative at point $\mathbf{x}_\alpha$ through a linear mapping with a matrix $\mathbf{G}_\alpha$:

$$\left.\frac{\partial \phi}{\partial x_i}\right|_{\mathbf{x}_\alpha}^{(0)} = G_{ij,\alpha}^{-1} \left.\frac{\partial \phi}{\partial x_j}\right|_{\mathbf{x}_\alpha} + \mathcal{O}\left(h\right) \tag{15}$$

This matrix-operation can be interpreted as a linear transformation of the initial Green-Gauss gradient, such that it can serve as derivative for an underlying reconstruction function that satisfies the conservation of the mean with an accuracy of $\mathcal{O}(h^2)$. Note, that if $G_{ij,\alpha}^{-1}$ equals a unit matrix δ_{ij}, the initial gradient

operator satisfies this condition inherently and thus features an error of $\mathcal{O}(h)$. This is the case, if the domain is discretized on a regular cartesian grid. Grid deformations lead $G^{-1}_{ij,\alpha}$ to deviate from δ_{ij}, which causes a constant error to manifest in equation (15). Note that this is a fundamental difference to node-centered edge-based methods, for which the Green-Gauss gradient from equation (10) is exact for linear functions on arbitrary triangular/tetrahedral grids [51, 52]. It can be shown that the inverse of the correction matrix $\mathbf{G}_\alpha$ is calculated from a Green-Gauss gradient of the first geometric volume moment tensor of Ω_α

$$G^{-1}_{ij,\alpha} := \left.\frac{\partial \mathcal{M}_j}{\partial x_i}\right|^{(0)}_{\mathbf{x}_\alpha} \qquad \text{with} \qquad \left.\frac{\partial \mathcal{M}_j}{\partial x_i}\right|^{(0)}_{\mathbf{x}_\alpha} := \frac{1}{|\Omega_\alpha|} \sum_{\beta \in \mathbb{V}^{(1)}_\alpha} \frac{1}{2} \left(\mathcal{M}^{(\beta,\alpha)}_j + \mathcal{M}^{(\alpha,\alpha)}_j \right) \mathcal{S}^{(\alpha\beta)}_i . \tag{16}$$

This simply refers to the application of the operator in equation (10) on the respective tensor entries. It must be noticed, that the centering of the volume moments in equation (16) varies according to the respective element Ω_α, where relation (9a) can be used. Incorporating the rank one moment tensor into matrix $\mathbf{G}_\alpha$ is one major difference towards the cell-centered approach, described in the work of Pont et al. [13]. In a cell-centered approach, the data is stored at the geometric centroids of primary grid elements, leading to the fact that rank one geometric volume moments reduce to zero. In contrast, elements in an edge-based representation feature a higher complexity in terms of their shape. If the flow data is stored at the primary grid nodes $\mathbf{x}_\alpha$, which generally do not coincide with the geometric centroid of a median-dual element, the condition $\mathcal{M}^{(\alpha,\alpha)}_i = 0$ is violated and must be taken into account. This is done inherently by the definition of matrix $\mathbf{G}_\alpha$. Thus, the proposed method gives the opportunity to store the cell-averaged solution at any point within element Ω_α while preserving the order of accuracy. Finally, the matrix is used to introduce a 1-exact gradient operator, which is calculated by

$$\left.\frac{\partial \phi}{\partial x_i}\right|^{(1)}_{\mathbf{x}_\alpha} := G_{ij,\alpha} \left.\frac{\partial \phi}{\partial x_j}\right|^{(0)}_{\mathbf{x}_\alpha} \qquad \text{where} \qquad \left.\frac{\partial \phi}{\partial x_i}\right|^{(1)}_{\mathbf{x}_\alpha} = \delta_{ij} \left.\frac{\partial \phi}{\partial x_j}\right|_{\mathbf{x}_\alpha} + \mathcal{O}\left(h\right). \tag{17}$$

It is used to approximate the solution in the vicinity of Ω_α with a 1-exact reconstruction polynomial

$$\phi^{(2)}(\mathbf{x};\mathbf{x}_\alpha) = \phi\Big|^{(2)}_{\mathbf{x}_\alpha} + \left.\frac{\partial \phi}{\partial x_i}\right|^{(1)}_{\mathbf{x}_\alpha} (x_i - x_{i,\alpha}) \qquad \text{with} \qquad \phi\Big|^{(2)}_{\mathbf{x}_\alpha} = \overline{\phi}_\alpha - \left.\frac{\partial \phi}{\partial x_i}\right|^{(1)}_{\mathbf{x}_\alpha} \mathcal{M}^{(\alpha,\alpha)}_i . \tag{18}$$

2.2. 2-exact reconstruction

If the solution is to be approximated by a 2-exact reconstruction polynomial, a second derivative of appropriate order of accuracy is required. It is obtained by applying the Green-Gauss operator (10) on the 1-exact gradient of ϕ. This leads to an approximate Hessian matrix which features an error of $\mathcal{O}(1)$ on deformed grids

$$\left.\frac{\partial^2 \phi}{\partial x_i \partial x_j}\right|^{(0)}_{\mathbf{x}_\alpha} := \frac{1}{|\Omega_\alpha|} \sum_{\beta \in \mathbb{V}^{(1)}_\alpha} \frac{1}{2} \left(\left.\frac{\partial \phi}{\partial x_i}\right|^{(1)}_{\mathbf{x}_\alpha} + \left.\frac{\partial \phi}{\partial x_i}\right|^{(1)}_{\mathbf{x}_\beta} \right) \mathcal{S}^{(\alpha\beta)}_j \tag{19}$$

Similar to the gradient, there exists a linear mapping, which can be used to correct this Hessian matrix to a form that ensures an accuracy of $\mathcal{O}(h)$ on arbitrary grids. The starting point is a Taylor series expansion of second degree for the solution ϕ around a primary grid node $\mathbf{x}_\alpha$:

$$\phi(\mathbf{x}) = \phi\Big|_{\mathbf{x}_\alpha} + \left.\frac{\partial \phi}{\partial x_i}\right|_{\mathbf{x}_\alpha} (x_i - x_{i,\alpha}) + \frac{1}{2} \left.\frac{\partial^2 \phi}{\partial x_i \partial x_j}\right|_{\mathbf{x}_\alpha} (x_i - x_{i,\alpha})\,(x_j - x_{j,\alpha}) + \mathcal{O}\left(h^3\right). \tag{20}$$

By volume-averaging equation (20) on Ω_α and Ω_β, the available averages can be expressed by

$$\overline{\phi}_\alpha = \phi\Big|_{\mathbf{x}_\alpha} + \left.\frac{\partial \phi}{\partial x_i}\right|_{\mathbf{x}_\alpha} \mathcal{M}^{(\alpha,\alpha)}_i + \frac{1}{2} \left.\frac{\partial^2 \phi}{\partial x_i \partial x_j}\right|_{\mathbf{x}_\alpha} \mathcal{M}^{(\alpha,\alpha)}_{ij} + \mathcal{O}\left(h^3\right), \tag{21}$$

$$\overline{\phi}_\beta = \phi\Big|_{\mathbf{x}_\alpha} + \frac{\partial \phi}{\partial x_i}\Big|_{\mathbf{x}_\alpha} \mathcal{M}_i^{(\beta,\alpha)} + \frac{1}{2}\frac{\partial^2 \phi}{\partial x_i \partial x_j}\Big|_{\mathbf{x}_\alpha} \mathcal{M}_{ij}^{(\beta,\alpha)} + \mathcal{O}\left(h^3\right). \tag{22}$$

After inserting these expressions for $\overline{\phi}_\alpha$ and $\overline{\phi}_\beta$ into the 1-exact gradient operator (17), it can be shown that the leading error term of the 1-exact gradient rises with the second derivative of ϕ at $\mathbf{x}_\alpha$ according to

$$\frac{\partial \phi}{\partial x_i}\Big|_{\mathbf{x}_\alpha}^{(1)} = \frac{\partial \phi}{\partial x_i}\Big|_{\mathbf{x}_\alpha} + \frac{1}{2}\frac{\partial^2 \phi}{\partial x_j \partial x_k}\Big|_{\mathbf{x}_\alpha} \frac{\partial \mathcal{M}_{jk}}{\partial x_i}\Big|_{\mathbf{x}_\alpha}^{(1)} + \mathcal{O}\left(h^2\right), \tag{23}$$

where the 1-exact gradient of the rank two geometric volume moments has been introduced as

$$\frac{\partial \mathcal{M}_{mn}}{\partial x_i}\Big|_{\mathbf{x}_\alpha}^{(1)} := \frac{G_{ij,\alpha}}{|\Omega_\alpha|} \sum_{\beta \in \mathbb{V}_\alpha^{(1)}} \frac{1}{2}\left(\mathcal{M}_{mn}^{(\beta,\alpha)} + \mathcal{M}_{mn}^{(\alpha,\alpha)}\right) \mathcal{S}_j^{(\alpha\beta)}. \tag{24}$$

This quantity lies in the order of magnitude of $\mathcal{O}(h)$. Thus, if the second derivative of ϕ is estimated with an accuracy of $\mathcal{O}(h)$, it can be used to correct the 1-exact gradient operator to reach an accuracy of $\mathcal{O}(h^2)$. This successive correction of derivatives is the key in the multiple-correction approach to reach higher levels of accuracy, while information is only exchanged among adjacent elements. To obtain a correction procedure for the Hessian matrix (19), the 1-exact gradient at position $\mathbf{x}_\beta$ must be expressed similar to the derivative in (23)

$$\frac{\partial \phi}{\partial x_i}\Big|_{\mathbf{x}_\beta}^{(1)} = \frac{\partial \phi}{\partial x_i}\Big|_{\mathbf{x}_\alpha} + \frac{\partial^2 \phi}{\partial x_i \partial x_j}\Big|_{\mathbf{x}_\alpha} (x_{j,\,\beta} - x_{j,\alpha}) + \frac{1}{2}\frac{\partial^2 \phi}{\partial x_j \partial x_k}\Big|_{\mathbf{x}_\alpha} \frac{\partial \mathcal{M}_{jk}}{\partial x_i}\Big|_{\mathbf{x}_\beta}^{(1)} + \mathcal{O}\left(h^2\right), \tag{25}$$

The analytic derivatives at $\mathbf{x}_\beta$ have been expressed through derivatives at $\mathbf{x}_\alpha$ for which the underlying Taylor-polynomial (20) has been exploited. The relation is finally inserted into the Hessian operator (19)

$$\frac{\partial^2 \phi}{\partial x_i x_j}\Big|_{\mathbf{x}_{\mathbf{x}_\alpha}}^{(0)} = \frac{\partial^2 \phi}{\partial x_i \partial x_k}\Big|_{\mathbf{x}_\alpha} \frac{\partial x_k}{\partial x_j}\Big|_{\mathbf{x}_\alpha}^{(0)} + \frac{1}{2}\frac{\partial^2 \phi}{\partial x_m \partial x_n}\Big|_{\mathbf{x}_\alpha} \frac{\partial^2 \mathcal{M}_{mn}}{\partial x_i \partial x_j}\Big|_{\mathbf{x}_\alpha}^{(0)} + \mathcal{O}\left(h\right), \tag{26}$$

with the Green-Gauss derivative operators for x_k and $\mathcal{M}_{mn}$

$$\frac{\partial x_k}{\partial x_j}\Big|_{\mathbf{x}_\alpha}^{(0)} := \frac{1}{|\Omega_\alpha|} \sum_{\beta \in \mathbb{V}_\alpha^{(1)}} \frac{1}{2}\left(x_{k,\alpha} + x_{k,\,\beta}\right) \mathcal{S}_j^{(\alpha\beta)}, \tag{27}$$

$$\frac{\partial^2 \mathcal{M}_{mn}}{\partial x_i \partial x_j}\Big|_{\mathbf{x}_\alpha}^{(0)} := \frac{1}{|\Omega_\alpha|} \sum_{\beta \in \mathbb{V}_\alpha^{(1)}} \frac{1}{2}\left(\frac{\partial \mathcal{M}_{mn}}{\partial x_i}\Big|_{\mathbf{x}_\alpha}^{(1)} + \frac{\partial \mathcal{M}_{mn}}{\partial x_i}\Big|_{\mathbf{x}_\beta}^{(1)}\right) \mathcal{S}_j^{(\alpha\beta)}. \tag{28}$$

The linear mapping in equation (26) can be expressed in terms of a matrix multiplication by vectorizing the Hessian matrices. The vectorized Hessian will be denoted by $\widehat{\mathbf{D}}_\alpha(\phi)$ and all matrix entries are arranged in the following order, as shown for the approximate Hessian matrix:

$$\widehat{\mathbf{D}}_\alpha^{(0)}(\phi) = \left[\, \frac{\partial^2 \phi}{\partial x_1 \partial x_1}\Big|_{\mathbf{x}_\alpha}^{(0)} \quad \frac{\partial^2 \phi}{\partial x_1 \partial x_2}\Big|_{\mathbf{x}_\alpha}^{(0)} \quad \frac{\partial^2 \phi}{\partial x_1 \partial x_3}\Big|_{\mathbf{x}_\alpha}^{(0)} \quad \frac{\partial^2 \phi}{\partial x_2 \partial x_2}\Big|_{\mathbf{x}_\alpha}^{(0)} \quad \frac{\partial^2 \phi}{\partial x_2 \partial x_3}\Big|_{\mathbf{x}_\alpha}^{(0)} \quad \frac{\partial^2 \phi}{\partial x_3 \partial x_3}\Big|_{\mathbf{x}_\alpha}^{(0)} \,\right]. \tag{29}$$

Considering the symmetry of the Hessian matrix, it is now possible to obtain a correction matrix $H_{ij,\alpha}$ to relate the approximate Hessian matrix operator $\widehat{\mathbf{D}}_{\alpha}^{(0)}(\phi)$ to its analytical counterpart $\widehat{\mathbf{D}}_{\alpha}(\phi)$

$$\widehat{D}_{i,\alpha}^{(0)}(\phi) = H_{ij,\alpha}^{-1}\, \widehat{D}_{j,\alpha}(\phi) + \mathcal{O}\left(h\right). \tag{30}$$

It is shown in Appendix A how the entries of matrix $H_{ij,\alpha}^{-1}$ are calculated. Just like $\mathbf{G}_{\alpha}$, matrix $\mathbf{H}_{\alpha}$ depends solely on the mesh geometry and thus can be calculated and inverted prior to the simulation. It also reduces to a unit matrix δ_{ij} for regular cartesian grids. Finally, a 2-exact Hessian matrix operator is introduced as

$$\widehat{D}_{i,\alpha}^{(1)}(\phi) := H_{ij,\alpha}\, \widehat{D}_{j,\alpha}^{(0)}(\phi). \tag{31}$$

During runtime, it is only necessary to compute this matrix-vector product, in order to correct the Hessian operator (19) onto its 2-exact form. Since this Hessian operator features an accuracy of $\mathcal{O}(h)$, it can be employed to correct the 1-exact gradient according to equation (23). This leads to the definition of the 2-exact gradient operator

$$\left.\frac{\partial \phi}{\partial x_i}\right|_{\mathbf{x}_\alpha}^{(2)} := \left.\frac{\partial \phi}{\partial x_i}\right|_{\mathbf{x}_\alpha}^{(1)} - \frac{1}{2}\left.\frac{\partial^2 \phi}{\partial x_j \partial x_k}\right|_{\mathbf{x}_\alpha}^{(1)} \left.\frac{\partial \mathcal{M}_{jk}}{\partial x_i}\right|_{\mathbf{x}_\alpha}^{(1)}. \tag{32}$$

The 1-exact gradient of the rank two volume moments must be stored in addition to the defined correction matrices for every primary grid node. It is also calculated only once prior to the simulation, if no mesh deformation is considered. Finally, the 2-exact reconstruction polynomial can be estimated according to

$$\phi^{(3)}(\mathbf{x};\mathbf{x}_\alpha) = \phi\Big|_{\mathbf{x}_\alpha}^{(3)} + \left.\frac{\partial \phi}{\partial x_i}\right|_{\mathbf{x}_\alpha}^{(2)} (x_i - x_{i,\alpha}) + \frac{1}{2}\left.\frac{\partial^2 \phi}{\partial x_i \partial x_j}\right|_{\mathbf{x}_\alpha}^{(1)} (x_i - x_{i,\alpha})\,(x_j - x_{j,\alpha})\,, \tag{33}$$

where the point value of ϕ at $\mathbf{x}_\alpha$ is approximated according to equation (7) with

$$\phi\Big|_{\mathbf{x}_\alpha}^{(3)} = \overline{\phi}_\alpha - \left.\frac{\partial \phi}{\partial x_i}\right|_{\mathbf{x}_\alpha}^{(2)} \mathcal{M}_i^{(\alpha,\alpha)} - \frac{1}{2}\left.\frac{\partial^2 \phi}{\partial x_i \partial x_j}\right|_{\mathbf{x}_\alpha}^{(1)} \mathcal{M}_{ij}^{(\alpha,\alpha)}. \tag{34}$$

The overall procedure to obtain a 2-exact reconstruction of ϕ in the entire domain is summarized in algorithm 1.

2.3. Reconstruction at boundaries

A problem of the median-dual representation is that primary grid nodes at boundaries are not located in the interior of their associated median-dual elements, but rather directly on the element boundary-interface. This is particularly undesirable at solid walls and can lead to problems at sharp corners [50]. To avoid these issues, certain boundary-vertices are shifted into the domain. The shifting of a boundary node $\mathbf{x}_\alpha$ is applied by translating it towards the interior of the domain and normal to the adjacent boundary face. This is done prior to the construction of the median-dual representation and affects the shape and size of the respective boundary element Ω_α, as well as its direct neighboring elements. This is indicated in Figure 2 for a primary grid of triangles. Boundary nodes are only shifted, when they are adjacent to wall boundary conditions, inlets or outlets. In contrast, vertices at symmetry boundary conditions remain. Note, that all boundaries are represented exclusively by planar triangles or quadrilaterals. This discrete approximation of boundaries inherently introduces an error of $\mathcal{O}\left(h^2\right)$ [19]. Both shifted and non-shifted boundaries affect the calculation of the k-exact correction matrices, since the latter depend on derivatives of the geometric volume moment tensors and these in turn get affected by boundaries. The influence of boundaries on the 1-exact

Algorithm 1 Procedure for obtaining a 2-exact reconstruction of a field variable ϕ.

procedure RECONSTRUCT SOLUTION 2-EXACT($\overline{\phi}$)
  for $\alpha \leftarrow 1$ to N **do**
    Compute approximate Green-Gauss operator $\left.\frac{\partial \phi}{\partial x_i}\right|_{\mathbf{x}_\alpha}^{(0)}$ from equation (10)
    Obtain 1-exact gradient $\left.\frac{\partial \phi}{\partial x_i}\right|_{\mathbf{x}_\alpha}^{(1)}$ through correction with matrix $G_{ij,\alpha}$ (17)
    Compute approximate Hessian matrix operator $\left.\frac{\partial^2 \phi}{\partial x_i \partial x_j}\right|_{\mathbf{x}_\alpha}^{(0)}$ from equation (19)
    Obtain 2-exact Hessian matrix $\left.\frac{\partial^2 \phi}{\partial x_i \partial x_j}\right|_{\mathbf{x}_\alpha}^{(1)}$ through correction with matrix $H_{ij,\alpha}$ (31)
    Correction for 2-exact gradient $\left.\frac{\partial \phi}{\partial x_i}\right|_{\mathbf{x}_\alpha}^{(2)}$ using 2-exact Hessian matrix (32)
    Reconstruct 2-exact point value $\left.\phi\right|_{\mathbf{x}_\alpha}^{(3)}$ at primary grid nodes $\mathbf{x}_\alpha$ (34)
    $\phi^{(3)}(\mathbf{x}; \mathbf{x}_\alpha) \leftarrow$ 2-exact reconstruction polynomial on Ω_α (33)
  return

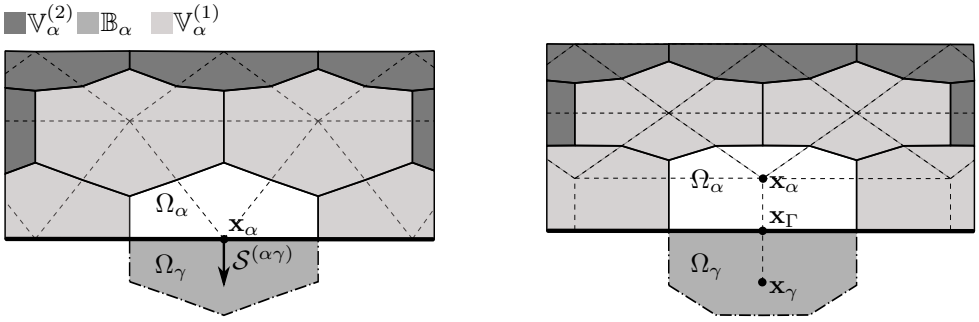

(a) Non-shifted boundaries (b) Shifted boundaries

Figure 2: Median-dual representation at boundaries. Dashed lines refer to the primary grid and thin solid lines to its respective median-dual representation. The thick solid line highlights the boundary. The area enclosed by the dash-dotted line shows a ghost element Ω_γ that is adjacent to the element Ω_α of the respective boundary node $\mathbf{x}_\alpha$. For shifted boundary elements, $\mathbf{x}_\Gamma$ denotes a point on the boundary surface $A_{\alpha\gamma}$ between Ω_α and Ω_γ. The solution of a ghost element Ω_γ is stored at $\mathbf{x}_\gamma$.

reconstruction can be taken into consideration through an additional term in the gradient operator (10)

$$\left.\frac{\partial \phi}{\partial x_i}\right|_{\mathbf{x}_\alpha}^{(0)} := \frac{1}{|\Omega_\alpha|} \sum_{\beta \in \mathbb{V}_\alpha^{(1)}} \frac{1}{2} \left(\overline{\phi}_\alpha + \overline{\phi}_\beta\right) \mathcal{S}_i^{(\alpha\beta)} + \frac{1}{|\Omega_\alpha|} \sum_{\gamma \in \mathbb{B}_\alpha} \left.\phi\right|_{\mathbf{x}_\Gamma} \mathcal{S}_i^{(\alpha\gamma)}. \tag{35}$$

Here, $\mathbb{B}_\alpha$ includes the neighborhood of boundary ghost elements Ω_γ adjacent to Ω_α. In this context, the position $\mathbf{x}_\Gamma$ refers to the centroid of the boundary face $A_{\alpha\gamma}$ and $\left.\phi\right|_{\mathbf{x}_\Gamma}$ indicates a prescribed boundary value. For non-shifted boundaries $\mathbf{x}_\alpha$ coincides with $\mathbf{x}_\Gamma$, as well as with node $\mathbf{x}_\gamma$ at which the solution of the adjacent ghost element Ω_γ is stored. This can be incorporated into matrix $G_{ij,\alpha}$, if the value $\left.\phi\right|_{\mathbf{x}_\Gamma}$ is calculated according to

$$\left.\phi\right|_{\mathbf{x}_\Gamma} = \frac{1}{2} \left(\overline{\phi}_\alpha + \overline{\phi}_\gamma\right) + \mathcal{O}\left(h\right). \tag{36}$$

As a result, the respective ghost elements Ω_γ can be included in the gradient calculation of the rank one volume moment tensor (16) similarly to interior elements. The volume moments of these non-shifted boundary ghost cells Ω_γ are deduced by mirroring the volume moments of the inner element Ω_α at the boundary face $A_{\alpha\gamma}$ with a rotation matrix R_{ij}

$$\mathcal{M}_i^{(\gamma,\gamma)} = R_{ij}\mathcal{M}_j^{(\alpha,\alpha)} \quad \text{with} \quad R_{ij} = \delta_{ij} - 2\frac{\mathcal{S}_i^{(\alpha\gamma)}\mathcal{S}_j^{(\alpha\gamma)}}{\mathcal{S}_k^{(\alpha\gamma)}\mathcal{S}_k^{(\alpha\gamma)}}. \tag{37}$$

At shifted boundaries, the presence of boundary ghost cells Ω_γ is neglected and the value $\phi|_{\mathbf{x}_\Gamma}$ is expressed at the boundary face in terms of a 1-exact Taylor polynomial

$$\phi\Big|_{\mathbf{x}_\Gamma} = \phi\Big|_{\mathbf{x}_\alpha} + \frac{\partial\phi}{\partial x_i}\Big|_{\mathbf{x}_\alpha}(x_{i,\gamma} - x_{i,\alpha}) + \mathcal{O}\left(h^2\right) \tag{38}$$

This term is substituted into the Green-Gauss gradient operator (10), leading to the following correction term

$$B_{ij,\alpha} = \frac{1}{|\Omega_\alpha|}\sum_{\gamma\in\mathbb{B}_\alpha}(x_{j,\gamma} - x_{j,\alpha})\,\mathcal{S}_i^{(\alpha\gamma)}, \tag{39}$$

that must be added to the inverse of matrix $G^{-1}_{ij,\alpha}$ in equation (16). The consideration of boundaries for the Hessian operator is more challenging, since this requires the knowledge of derivatives of flow quantities in the ghost cells. To circumvent this, interior gradients are simply extrapolated onto the nodes of boundary ghost cells $\mathbf{x}_\gamma$. The approximate Hessian operator (19) can then be extended with the following boundary contribution

$$\frac{\partial^2\phi}{\partial x_i x_j}\bigg|^{(0)}_{\mathbf{x}_\alpha} := \frac{1}{|\Omega_\alpha|}\sum_{\beta\in\mathbb{V}_\alpha^{(1)}}\frac{1}{2}\left(\frac{\partial\phi}{\partial x_i}\bigg|^{(1)}_{\mathbf{x}_\alpha} + \frac{\partial\phi}{\partial x_i}\bigg|^{(1)}_{\mathbf{x}_\beta}\right)\mathcal{S}_j^{(\alpha\beta)} + \frac{1}{|\Omega_\alpha|}\sum_{\gamma\in\mathbb{B}_\alpha}\frac{1}{2}\left(\frac{\partial\phi}{\partial x_i}\bigg|^{(1)}_{\mathbf{x}_\alpha} + \frac{\partial\phi}{\partial x_i}\bigg|^{(1)}_{\mathbf{x}_\gamma}\right)\mathcal{S}_j^{(\alpha\gamma)}. \tag{40}$$

With this approach boundaries can simply be taken into account for the correction matrix $H_{ij,\alpha}$ by providing further information on the rank two volume moment tensors $\mathcal{M}_{ij}^{(\gamma,\gamma)}$ of the ghost cells Ω_γ. These are then used in the calculation of the respective moment tensor derivatives in equations (24) and (28). For the actual gradient computation, the approximation of the ghost cell gradient $\frac{\partial\phi}{\partial x_i}\big|^{(1)}_{\mathbf{x}_\gamma}$ depends on the boundary treatment. Since non-shifted boundaries are used for symmetry conditions, the gradient is mirrored at such boundary interfaces.

$$\frac{\partial\phi}{\partial x_i}\bigg|^{(1)}_{\mathbf{x}_\gamma} = R_{ij}\,\frac{\partial\phi}{\partial x_j}\bigg|^{(1)}_{\mathbf{x}_\alpha}. \tag{41}$$

For shifted boundaries the gradient is extrapolated from the interior element Ω_α and its first neighborhood $\mathbb{V}_\alpha^{(1)}$:

$$\frac{\partial\phi}{\partial x_i}\bigg|^{(1)}_{\mathbf{x}_\gamma} = \frac{\partial\phi}{\partial x_i}\bigg|^{(1)}_{\mathbf{x}_\alpha} + \left[\frac{1}{|\Omega_\alpha|}\sum_{\beta\in\mathbb{V}_\alpha^{(1)}}\frac{1}{2}\left(\frac{\partial\phi}{\partial x_i}\bigg|^{(1)}_{\mathbf{x}_\alpha} + \frac{\partial\phi}{\partial x_i}\bigg|^{(1)}_{\mathbf{x}_\beta}\right)\mathcal{S}_j^{(\alpha\beta)}\right](x_{j,\gamma} - x_{j,\alpha}). \tag{42}$$

The proposed approach adjusts correction matrices in the vicinity of boundaries, so that the levels of accuracy for derivatives are formally maintained for boundary elements. This also affects correction matrices of elements that are not directly located at the domain boundaries. A drawback is that the solution near boundaries is essentially reconstructed on a stencil with fewer elements. This makes it prone to the occurrence

of instabilities, which was found particularly for shifted boundaries in connection with strong gradients. As a remedy, correction matrices at shifted boundaries are replaced by unit matrices, in order to overcome these stability problems. This reduces the accuracy of the calculated derivatives of boundary elements, since they are essentially calculated from the standard Green-Gauss procedures given in equation (10) and (19). The ghost cell correction for volume moment gradients is still employed, since it also affects elements that are not directly located at the domain boundaries.

3. Approximation of face fluxes

Once the reconstruction polynomials are determined, the surface integrals of equation (3) must be evaluated at element interfaces. In the scope of k-exact higher-order methods, this is generally done by reconstructing the flux function on the face at several quadrature points, in order to maintain the desired order of accuracy [17, 31, 58, 60, 61]. A drawback of this method is, that the number of quadrature points rises rapidly for the employed median-dual grid representation, where faces are compounds of several sub-triangles. In addition, to integrate this approach into an existing finite-volume solver, the underlying code structure must be modified significantly. Instead, a single-point surface integration method is applied in this work, which has also been successfully applied by Pont et al. [33] and Menasria et al. [35] for cell-centered grids. Furthermore, it was shown in the author's previous work [62, 63] that it is possible to employ this method for median-dual grids in $d = 2$. The approach is based on a Taylor series expansion around a single point $\mathbf{x}_\Gamma$ on a median-dual face $A_{\alpha\beta}$. The surface-integral of any flux function f_i can then be approximated by means of the reconstructed value $f_{\Gamma,i}$ and its derivatives at point $\mathbf{x}_\Gamma$:

$$\iint_{A_{\alpha\beta}} f_i \, n_i \, \mathrm{d}A = f_i \Big|_{\mathbf{x}_\Gamma} \mathcal{S}_i^{(\alpha\beta)} + \frac{\partial f_i}{\partial x_{j_1}}\bigg|_{\mathbf{x}_\Gamma} \mathcal{S}_{i,j_1}^{(\alpha\beta)} + \ldots + \frac{1}{k!} \frac{\partial^k f_i}{\partial x_{j_1} \ldots \partial x_{j_k}}\bigg|_{\mathbf{x}_\Gamma} \mathcal{S}_{i,j_1\ldots j_k}^{(\alpha\beta)} + \mathcal{O}\left(h^{k+1}\right). \tag{43}$$

This integration method relies on the definition of the rank p geometric surface moments, which give the opportunity to approximate the surface-integral with a higher order of accuracy regardless of the shape of the underlying primary grid elements. This can be achieved with only a single point of evaluation, whose position can be chosen arbitrarily on the surface. The surface moments are generally defined for a face $A_{\alpha\beta}$ by

$$\mathcal{S}_{i,j_1 j_2 \ldots j_p}^{(\alpha\beta)} = \iint_{A_{\alpha\beta}} n_i \left(x_{j_1} - x_{j_1,\Gamma}\right)\left(x_{j_2} - x_{j_2,\Gamma}\right) \ldots \left(x_{j_p} - x_{j_p,\Gamma}\right) \mathrm{d}A. \tag{44}$$

The subscripts i and j_p are separated by a comma to highlight that i indicates the face normal direction and j_p the spatial direction of the terms $\left(x_{j_p} - x_{j_p,\Gamma}\right)$. The superscripts $(\alpha\beta)$ indicate the elements Ω_α and Ω_β adjacent to the face, on which point $\mathbf{x}_\Gamma$ for the Taylor series expansion is located. The rank zero surface moments have already been introduced for the estimation of k-exact derivatives. The surface moments of a surface $A_{\alpha\beta}$ can be calculated from a weighted sum of the surface moments of its corresponding sub-triangles with their surface normals. This is done prior to the simulation. A detailed explanation on how to calculate geometric moments for triangular surfaces can be found in the literature [56]. Note that in contrast to the geometric volume moment formulation, the surface moments are not normalized with the interface area $|A_{\alpha\beta}|$. This is due to reasons of clarity for the further derivation of the scheme. It remains to reconstruct the unknown flux function $f_i|_{\mathbf{x}_\Gamma}$ and its derivatives at the cell interfaces. As it will be shown, these can be obtained from the already determined reconstruction polynomials of the adjacent elements.

3.1. Convective fluxes

In order to obtain a k-exact approximation of the convective fluxes $f_i = (u_i \phi)$, the primitive field variables u_i and ϕ are simply substituted by means of their reconstruction polynomials. The resulting product of these functions is then evaluated at $\mathbf{x}_\Gamma$. This is done similarly for the derivatives of f_i, where derivatives of the reconstruction polynomials are employed. After some algebra, it is possible to reformulate the convective

fluxes in terms of 2-exact reconstructed primitive field variables u_i and ϕ as:

$$\iint_{A_{\alpha\beta}} (u_i\phi)\, n_i \,\mathrm{d}A = \dot{m}\Big|_{\mathbf{x}_\Gamma}^{(3)} \phi\Big|_{\mathbf{x}_\Gamma}^{(3)} + \dot{m}_i\Big|_{\mathbf{x}_\Gamma}^{(3)} \frac{\partial\phi}{\partial x_i}\Big|_{\mathbf{x}_\Gamma}^{(2)} + \frac{1}{2}\dot{m}_{ij}\Big|_{\mathbf{x}_\Gamma}^{(3)} \frac{\partial^2\phi}{\partial x_i\partial x_j}\Big|_{\mathbf{x}_\Gamma}^{(1)} + |A_{\alpha\beta}|\,\mathcal{O}\left(h^3\right), \tag{45}$$

where the mass flux terms $\dot{m}$ have been defined by

$$\dot{m}\Big|_{\mathbf{x}_\Gamma}^{(3)} = u_i\Big|_{\mathbf{x}_\Gamma}^{(3)} \mathcal{S}_i^{(\alpha\beta)} + \frac{\partial u_i}{\partial x_j}\Big|_{\mathbf{x}_\Gamma}^{(2)} \mathcal{S}_{i,j}^{(\alpha\beta)} + \frac{1}{2}\frac{\partial^2 u_i}{\partial x_j\partial x_k}\Big|_{\mathbf{x}_\Gamma}^{(1)} \mathcal{S}_{i,jk}^{(\alpha\beta)}, \tag{46a}$$

$$\dot{m}_i\Big|_{\mathbf{x}_\Gamma}^{(3)} = u_j\Big|_{\mathbf{x}_\Gamma}^{(3)} \mathcal{S}_{j,i}^{(\alpha\beta)} + \frac{\partial u_j}{\partial x_k}\Big|_{\mathbf{x}_\Gamma}^{(2)} \mathcal{S}_{j,ki}^{(\alpha\beta)}, \tag{46b}$$

$$\dot{m}_{ij}\Big|_{\mathbf{x}_\Gamma}^{(3)} = u_k\Big|_{\mathbf{x}_\Gamma}^{(3)} \mathcal{S}_{k,ij}^{(\alpha\beta)}. \tag{46c}$$

Note that all these terms scale with $|A_{\alpha\beta}|$, due to the surface integration and the respective definition of the geometric surface moment tensors. Furthermore, the mass flux terms (46b) and (46c) scale also with h and h^2, respectively, which leads to the overall accuracy of $\mathcal{O}(h^3)$. The mass flux tensors at the interface node $\mathbf{x}_\Gamma$ are calculated with a central averaging of the reconstructed values from both adjacent elements. Note, that during the solution process this is done only once at the beginning of each time step t_n.

In the scope of inviscid compressible flows, convective numerical fluxes are typically evaluated as (approximate) solutions to local Riemann problems, exploiting the hyperbolic nature of the underlying equations. Unfortunately, this cannot be extended directly to fractional step approaches, since the system of equations are treated in a decoupled manner. Thus, to keep the numerical dissipation as small as possible, a central approximation of face values is employed, using the reconstruction functions of the adjacent elements. This method lacks to recognize and suppress odd-even decoupling of the solution [50]. Hence, to stabilize the solution process, the reconstruction of face values is biased towards the element in upwind direction. This acts as an artificial numerical dissipation term and has also been employed in several other works [13, 64, 65]. A detailed analysis on the spectral properties for this approach has been given by Pont et al. [13] for cell-centered grids. Finally, for a 2-exact reconstruction, the scalar field variable $\phi|_{\mathbf{x}_\Gamma}^{(3)}$ at the interface $A_{\alpha\beta}$ is finally approximated according to

$$\begin{aligned}\phi\Big|_{\mathbf{x}_\Gamma}^{(3)} = a_U\,\phi\Big|_{\mathbf{x}_U}^{(3)} + a_D\,\phi\Big|_{\mathbf{x}_D}^{(3)} + \left(b_U\,\frac{\partial\phi}{\partial x_i}\Big|_{\mathbf{x}_U}^{(2)} + b_D\,\frac{\partial\phi}{\partial x_i}\Big|_{\mathbf{x}_D}^{(2)}\right)\Delta x_{i,DU} \\ + \left(c_U\,\frac{\partial^2\phi}{\partial x_i\partial x_j}\Big|_{\mathbf{x}_U}^{(1)} + c_D\,\frac{\partial^2\phi}{\partial x_i\partial x_j}\Big|_{\mathbf{x}_D}^{(1)}\right)\Delta x_{i,DU}\Delta x_{j,DU}.\end{aligned} \tag{47}$$

Here, U is the upwind and D the downwind direction at the interface and $\Delta x_{i,DU} = x_{i,D} - x_{i,U}$ denotes the distance vector from the upwind to the downwind node. Note that the point values $\phi|_{\mathbf{x}_U}^{(3)}$ and $\phi|_{\mathbf{x}_D}^{(3)}$ must be approximated from the underlying reconstruction polynomial according to equation (7). The derivatives of ϕ at the interface are reconstructed similarly

$$\frac{\partial\phi}{\partial x_i}\Big|_{\mathbf{x}_\Gamma}^{(2)} = a_U\,\frac{\partial\phi}{\partial x_i}\Big|_{\mathbf{x}_U}^{(2)} + a_D\,\frac{\partial\phi}{\partial x_i}\Big|_{\mathbf{x}_D}^{(2)} + \left(b_U\,\frac{\partial^2\phi}{\partial x_i\partial x_j}\Big|_{\mathbf{x}_U}^{(2)} + b_D\,\frac{\partial^2\phi}{\partial x_i\partial x_j}\Big|_{\mathbf{x}_D}^{(2)}\right)\Delta x_{j,DU}, \tag{48}$$

$$\frac{\partial^2\phi}{\partial x_i\partial x_j}\Big|_{\mathbf{x}_\Gamma}^{(1)} = a_U\,\frac{\partial^2\phi}{\partial x_i\partial x_j}\Big|_{\mathbf{x}_U}^{(1)} + a_D\,\frac{\partial^2\phi}{\partial x_i\partial x_j}\Big|_{\mathbf{x}_D}^{(1)}. \tag{49}$$

By adjustment of the coefficients a, b, c it is possible to blend between different discretization schemes. Table 1 shows parameters that lead to a 2-exact, a 1-exact and to two 0-exact schemes, namely the Low-Dissipation Low-Dispersion scheme (LD2) by Loewe et al. [66], as well as a conventional central differencing scheme (CDS). The latter are typically considered as second-order accurate finite-volume schemes, but are only first-order accurate on distorted grids. Thus, the 1-exact approach is already an improvement with respect to these conventional schemes, since the accuracy is maintained, regardless of the grid, as it will be demonstrated in Section 5. Depending on the exactness of the scheme, the respective correction operations on the derivatives are applied. For the 0-exact schemes, point values such as $\phi|_{\mathbf{x}_U}$ reduce to volume-averages $\overline{\phi}_U$ and only geometric surface moments of rank zero are used. The parameter $\theta \in [0, 1]$ is utilized for the 2- and 1-exact schemes to shift the bias towards the element in the upwind direction and thus stabilizing the solution. A value of $\theta = 0$ results in a central discretization, whereas with $\theta = 1$ the bias is set fully towards the upwind direction. In the entire work, a value of $\theta = 0.2$ is used. For all schemes, terms that contain derivatives are set to zero for the reconstruction of face-values adjacent to shifted elements. This increases the overall stability, especially for the 2-exact reconstruction, even though the reconstruction is formally first-order accurate at such faces. However, it was observed that this error does not significantly affect the solution in all the examined test cases that involve shifted boundaries.

Table 1: Parameters for the flux calculation with different discretization schemes.

Scheme	a_U	a_D	b_U	b_D	c_U	c_D
$k = 2$	$(1+\theta)/2$	$(1-\theta)/2$	$(1+\theta)/4$	$-(1-\theta)/4$	$(1+\theta)/16$	$(1-\theta)/16$
$k = 1$	$(1+\theta)/2$	$(1-\theta)/2$	$(1+\theta)/4$	$-(1-\theta)/4$	0	0
LD2	1/2	1/2	9/50	−9/50	0	0
CDS	1/2	1/2	0	0	0	0

3.2. Diffusive fluxes

For the diffusive fluxes $f_i = D(\partial\phi/\partial x_i)$ a classical scheme referred to as Mathur-Murthy [67, 68] or face-tangent scheme [59] will be used. This scheme is often employed for unstructured grids and is known to be second-order accurate in space. However, it will be shown that the median-dual representation introduces an error of $\mathcal{O}(h)$ on distorted grids. In the following, additional terms for the scheme are derived, which allow to overcome this error through a k-exact reconstruction. Starting point is an approximation of the surface-integral by means of equation (43)

$$\iint_{A_{\alpha\beta}} \left(D \frac{\partial \phi}{\partial x_i} \right) n_i \, \mathrm{d}A = D \left. \frac{\partial \phi}{\partial x_i} \right|_{\mathbf{x}_\Gamma} \mathcal{S}_i^{(\alpha\beta)} + D \left. \frac{\partial^2 \phi}{\partial x_i \partial x_j} \right|_{\mathbf{x}_\Gamma} \mathcal{S}_{i,j}^{(\alpha\beta)} + |A_{\alpha\beta}| \, \mathcal{O}\left(h^2\right). \tag{50}$$

Unlike for the convective fluxes, the surface-integral cannot be approximated with $\mathcal{O}\left(h^3\right)$. This would require the first and second derivatives of ϕ to have a higher exactness level, as well as a third derivative to be available with an accuracy of $\mathcal{O}(h)$. This can be provided with a 3-exact reconstruction, but is not investigated in this work. To prevent spurious oscillations, it is desired to express the first term on the right of equation (50) by means of the adjacent volume-averages $\overline{\phi}_\alpha$ and $\overline{\phi}_\beta$ [67]. This is achieved by splitting the joint face normal vector $\mathcal{S}_i^{(\alpha\beta)}$ in two parts

$$\left. \frac{\partial \phi}{\partial x_i} \right|_{\mathbf{x}_\Gamma} \mathcal{S}_i^{(\alpha\beta)} = \varepsilon^{(\alpha\beta)} \left(\left. \frac{\partial \phi}{\partial x_i} \right|_{\mathbf{x}_\Gamma} \Delta x_{i,\,\beta\alpha} \right) - \left. \frac{\partial \phi}{\partial x_i} \right|_{\mathbf{x}_\Gamma} \left(\varepsilon^{(\alpha\beta)} \Delta x_{i,\,\beta\alpha} - \mathcal{S}_i^{(\alpha\beta)} \right), \tag{51}$$

where the factor $\varepsilon^{(\alpha\beta)}$ is defined by

$$\varepsilon^{(\alpha\beta)} = \frac{\mathcal{S}_i^{(\alpha\beta)} \mathcal{S}_i^{(\alpha\beta)}}{\Delta x_{j,\,\beta\alpha} \, \mathcal{S}_j^{(\alpha\beta)}}. \tag{52}$$

The first term arises from the projection of the distance vector $\Delta x_{i,\,\beta\alpha} = x_{i,\,\beta} - x_{i,\alpha}$ onto the face normal $\mathcal{S}_i^{(\alpha\beta)}$, both pointing from element Ω_α to Ω_β. The second term contributes for the part of $\Delta x_{i,\,\beta\alpha}$ which is orthogonal to $\mathcal{S}_i^{(\alpha\beta)}$, as illustrated in Figure 3. It reduces to zero for orthogonal grids.

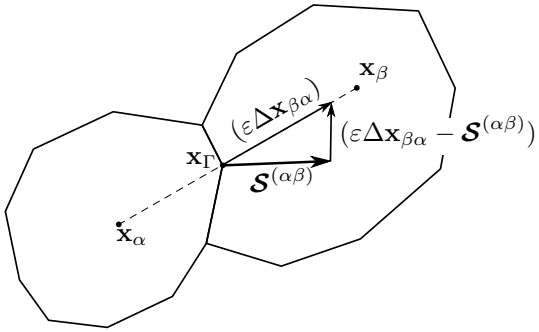

Figure 3: Splitting of the joint median-dual face normal $\mathcal{S}_i^{(\alpha\beta)}$ into a part $(\varepsilon^{(\alpha\beta)}\Delta x_{i,\,\beta\alpha})$ projected onto the distance vector $x_{i,\,\beta\alpha}$ and a part $(\varepsilon^{(\alpha\beta)}\Delta x_{i,\,\beta\alpha} - \mathcal{S}_i^{(\alpha\beta)})$ orthogonal to it.

The goal is to express the projection of the face-gradient on the vector $\Delta\mathbf{x}_{\beta\alpha}$ in equation (51) by means of the volume-averages $\overline{\phi}_\alpha$ and $\overline{\phi}_\beta$, which leads to a formulation that is especially robust for highly-skewed grids [51, 59]. However, it must be ensured that this formulation satisfies the constraints given from the k-exactness criteria (4) and (5). For the derivation of such a relation, a Taylor-series expansion is defined in the vicinity of node $\mathbf{x}_\Gamma$, which reads for $k = 2$:

$$\phi(\mathbf{x}) = \phi\Big|_{\mathbf{x}_\Gamma} + \frac{\partial\phi}{\partial x_i}\Big|_{\mathbf{x}_\Gamma}(x_i - x_{i,\Gamma}) + \frac{1}{2}\frac{\partial^2\phi}{\partial x_i\partial x_j}\Big|_{\mathbf{x}_\Gamma}(x_i - x_{i,\Gamma})(x_j - x_{j,\Gamma}) + \mathcal{O}\left(h^3\right). \tag{53}$$

This equation is volume-averaged in order to obtain expressions of averaged quantities of the adjacent elements that satisfy the conservation of the mean

$$\overline{\phi}_\alpha = \phi\Big|_{\mathbf{x}_\Gamma} + \frac{\partial\phi}{\partial x_i}\Big|_{\mathbf{x}_\Gamma}\mathcal{M}_i^{(\alpha,\Gamma)} + \frac{1}{2}\frac{\partial^2\phi}{\partial x_i\partial x_j}\Big|_{\mathbf{x}_\Gamma}\mathcal{M}_{ij}^{(\alpha,\Gamma)} + \mathcal{O}\left(h^3\right), \tag{54a}$$

$$\overline{\phi}_\beta = \phi\Big|_{\mathbf{x}_\Gamma} + \frac{\partial\phi}{\partial x_i}\Big|_{\mathbf{x}_\Gamma}\mathcal{M}_i^{(\beta,\Gamma)} + \frac{1}{2}\frac{\partial^2\phi}{\partial x_i\partial x_j}\Big|_{\mathbf{x}_\Gamma}\mathcal{M}_{ij}^{(\beta,\Gamma)} + \mathcal{O}\left(h^3\right). \tag{54b}$$

Taking into account the relations for the geometric volume moment tensors in equations (9), the face-gradient can be projected onto the distance vector $\Delta\mathbf{x}_{\beta\alpha}$ through

$$\begin{aligned}\frac{\partial\phi}{\partial x_i}\Big|_{\mathbf{x}_\Gamma}\Delta x_{i,\,\beta\alpha} = (\overline{\phi}_\beta - \overline{\phi}_\alpha) - \frac{\partial\phi}{\partial x_i}\Big|_{\mathbf{x}_\Gamma}\left(\mathcal{M}_i^{(\beta,\,\beta)} - \mathcal{M}_i^{(\alpha,\alpha)}\right) - \frac{1}{2}\frac{\partial^2\phi}{\partial x_i\partial x_j}\Big|_{\mathbf{x}_\Gamma}\left(\mathcal{M}_{ij}^{(\beta,\,\beta)} - \mathcal{M}_{ij}^{(\alpha,\alpha)}\right)\\ - \frac{1}{4}\frac{\partial^2\phi}{\partial x_i\partial x_j}\Big|_{\mathbf{x}_\Gamma}\left[\Delta x_{i,\,\beta\alpha}\left(\mathcal{M}_j^{(\alpha,\alpha)} + \mathcal{M}_j^{(\beta,\,\beta)}\right) + \Delta x_{j,\,\beta\alpha}\left(\mathcal{M}_i^{(\alpha,\alpha)} + \mathcal{M}_i^{(\beta,\,\beta)}\right)\right] + \mathcal{O}\left(h^3\right).\end{aligned} \tag{55}$$

Similar to the convective fluxes, the gradients at the face are approximated from the underlying k-exact reconstruction polynomials. For $k = 2$, using a central formulation leads to the following expressions for the

gradient and the Hessian matrix at the face

$$\left.\frac{\partial \phi}{\partial x_i}\right|_{\mathbf{x}_\Gamma} = \frac{1}{2}\left(\left.\frac{\partial \phi}{\partial x_i}\right|_{\mathbf{x}_\alpha}^{(2)} + \left.\frac{\partial \phi}{\partial x_i}\right|_{\mathbf{x}_\beta}^{(2)}\right) + \frac{1}{4}\left(\left.\frac{\partial^2 \phi}{\partial x_i \partial x_j}\right|_{\mathbf{x}_\alpha}^{(1)} - \left.\frac{\partial^2 \phi}{\partial x_i \partial x_j}\right|_{\mathbf{x}_\beta}^{(1)}\right) \Delta x_{j,\,\beta\alpha} + \mathcal{O}\left(h^2\right), \tag{56a}$$

$$\left.\frac{\partial^2 \phi}{\partial x_i \partial x_j}\right|_{\mathbf{x}_\Gamma} = \frac{1}{2}\left(\left.\frac{\partial^2 \phi}{\partial x_i \partial x_j}\right|_{\mathbf{x}_\alpha}^{(1)} + \left.\frac{\partial^2 \phi}{\partial x_i \partial x_j}\right|_{\mathbf{x}_\beta}^{(1)}\right) + \mathcal{O}\left(h\right). \tag{56b}$$

Equations (51), (55) and (56) are inserted into the diffusion flux integral (50), which finally leads to the expression

$$\iint_{A_{\alpha\beta}} \left(D\frac{\partial \phi}{\partial x_i}\right) n_i \,\mathrm{d}A = D\left[F_{D,MM}^{(\alpha\beta)} + F_{D,EX1}^{(\alpha\beta)} + F_{D,EX2}^{(\alpha\beta)}\right] + \left|A_{\alpha\beta}\right| \mathcal{O}\left(h^2\right). \tag{57}$$

The first term of equation (57) recovers the original formulation of Mathur and Murthy [67]

$$F_{D,MM}^{(\alpha\beta)} = \varepsilon^{(\alpha\beta)}\left(\overline{\phi}_\beta - \overline{\phi}_\alpha\right) - \frac{1}{2}\left(\left.\frac{\partial \phi}{\partial x_i}\right|_{\mathbf{x}_\alpha}^{(2)} + \left.\frac{\partial \phi}{\partial x_i}\right|_{\mathbf{x}_\beta}^{(2)}\right)\left(\varepsilon^{(\alpha\beta)}\Delta x_{i,\,\beta\alpha} - \mathcal{S}_i^{(\alpha\beta)}\right). \tag{58}$$

The terms $F_{D,EX1}^{(\alpha\beta)}$ and $F_{D,EX2}^{(\alpha\beta)}$ are designated as contributions to enhance the accuracy in the scope of the k-exact reconstruction approach. The term $F_{D,EX1}^{(\alpha\beta)}$ accounts for the 1-exactness reconstruction of the diffusion flux integral

$$F_{D,EX1}^{(\alpha\beta)} = -\frac{1}{2}\varepsilon^{(\alpha\beta)}\left(\left.\frac{\partial \phi}{\partial x_i}\right|_{\mathbf{x}_\alpha}^{(2)} + \left.\frac{\partial \phi}{\partial x_i}\right|_{\mathbf{x}_\beta}^{(2)}\right)\left(\mathcal{M}_i^{(\beta,\,\beta)} - \mathcal{M}_i^{(\alpha,\alpha)}\right). \tag{59}$$

This term compensates for an error of $\mathcal{O}\left(h\right)$ that results from the adjacent volume-averages not being stored in the respective geometric element centroids. This error is not present if the rank one volume moments in equation (59) reduce to zero. The latter is valid for cell-centered schemes, thus leading the standard Mathur-Murthy scheme to reconstruct the face-gradient with a second order of accuracy. The second correction term $F_{D,EX2}^{(\alpha\beta)}$ reduces this specific error even further to $\mathcal{O}\left(h^3\right)$ and contributes to approximate the surface-integral with $\mathcal{O}\left(h^2\right)$, regardless of the shape of $A_{\alpha\beta}$. However, it does not achieve an overall accuracy of $\mathcal{O}\left(h^3\right)$ due to the reasons mentioned above.

$$\begin{aligned} F_{D,EX2}^{(\alpha\beta)} = {} & \frac{1}{2}\left(\left.\frac{\partial^2 \phi}{\partial x_i \partial x_j}\right|_{\mathbf{x}_\alpha}^{(1)} + \left.\frac{\partial^2 \phi}{\partial x_i \partial x_j}\right|_{\mathbf{x}_\beta}^{(1)}\right)\left[\mathcal{S}_{i,j}^{(\alpha\beta)} - \frac{1}{2}\varepsilon^{(\alpha\beta)}\left(\mathcal{M}_{ij}^{(\beta,\,\Gamma)} - \mathcal{M}_{ij}^{(\alpha,\,\Gamma)}\right)\right] \\ & - \frac{1}{4}\left(\left.\frac{\partial^2 \phi}{\partial x_i \partial x_j}\right|_{\mathbf{x}_\alpha}^{(1)} - \left.\frac{\partial^2 \phi}{\partial x_i \partial x_j}\right|_{\mathbf{x}_\beta}^{(1)}\right)\left[\varepsilon^{(\alpha\beta)}\left(\Delta x_{i,\,\beta\alpha} + \mathcal{M}_i^{(\beta,\,\beta)} - \mathcal{M}_i^{(\alpha,\alpha)}\right) - \mathcal{S}_i^{(\alpha\beta)}\right]\Delta x_{j,\,\beta\alpha}, \end{aligned} \tag{60}$$

with

$$\mathcal{M}_{ij}^{(\beta,\,\Gamma)} - \mathcal{M}_{ij}^{(\alpha,\,\Gamma)} = \mathcal{M}_{ij}^{(\beta,\,\beta)} - \mathcal{M}_{ij}^{(\alpha,\alpha)} + \frac{1}{2}\Delta x_{i,\,\beta\alpha}\left(\mathcal{M}_j^{(\beta,\,\beta)} + \mathcal{M}_j^{(\alpha,\alpha)}\right) + \frac{1}{2}\Delta x_{j,\,\beta\alpha}\left(\mathcal{M}_i^{(\beta,\,\beta)} + \mathcal{M}_i^{(\alpha,\alpha)}\right). \tag{61}$$

3.3. Comparison of memory requirements between cell- and vertex-centered approaches

This section gives a brief overview on the memory requirements of a 2-exact vertex-centered multiple-correction approach compared to a cell-centered formulation, as for example given by Pont et al. [13]. A primary grid is considered, which consists of N_c control volumes, N_f faces, N_e edges and N_v vertices. The number of these entities can be related by Euler's formula $N_f + N_v = N_e + N_c$. Following the work of Barth [15], the number of control volumes for three dimensional meshes can be expressed using the number of vertices $N_c = \beta N_v$, where β usually ranges from five to seven for tetrahedral meshes. Similarly, the number

of faces can be calculated by that of the edges with $N_f = 2\beta/(1+\beta)N_e$. These formulas do not account for boundary-effects on the mesh structure. However, this influence can be neglected, since most primary grids of interest offer a high number of internal elements compared to those located at boundaries. Table 2 shows the number of additional floating point values to store, if the proposed reconstruction approach is implemented in a cell- or a vertex-centered representation and under consideration of symmetry properties for the moment tensors. The cell-centered approach stores volume moments and correction matrices for every control volume and surface moments for every face in the primary grid. As the solution is stored in the control volume centroids, the rank one geometric volume moment tensors reduce to zero. This also applies to the rank one geometric face moments $\mathcal{S}_{i,j}^{(\alpha\beta)}$, if $\mathbf{x}_\Gamma$ is chosen to be the geometric centroid of the interfaces. Contrary, in the median-dual approach volume moments must be calculated for every primary grid node and face moments for every primary grid edge and none of these can be neglected. By taking the sum over all values in Table 2 and employing the given grid-relations, the ratio for the number of additional values to store with the cell-centered representation $V_{\text{C-C}}$ to the number of additional values with the median-dual approach $V_{\text{M-D}}$ on an identical grid can be derived

$$\left(\frac{V_{\text{C-C}}}{V_{\text{M-D}}}\right) = \frac{101}{18} - \frac{505}{18(5+\beta)} \tag{62}$$

Compared to the median-dual approach, a cell-centered representation requires to store roughly three times as many additional floating point values for tetrahedral meshes on the same grid ($\beta \approx 6$). This ratio can only serve as a basic estimate and will definitely be smaller, when grids with mixed primary elements are considered. However, the ratio changes if both methods are compared for the same number of unknowns. In this case, the cell-centered approach requires roughly half as much memory as the vertex-centered method. For a better comparison of both methods in terms of memory, accuracy and performance, comparable studies can be performed as for example in the works of Diskin et al. [51, 69]. Besides this, the present multiple-correction approach offers reduced memory requirements compared to the vertex-centered method by Bernard et al. [36]. Their approach relies on a single 10×10 correction matrix to obtain a 2-exact reconstruction polynomial. It thus requires $100\,N_v$ additional floating point values to store this matrix, as well as the respective volume and surface moments. In contrast, our approach requires only $63\,N_v$ floating point values for both correction matrices and the gradient of the rank two geometric volume tensor, besides the additional moment invariants.

Table 2: Number of additional floating point values to store for the 2-exact multiple-correction scheme using a cell- or vertex-centered grid representation on an identical grid.

Representation	$\mathcal{M}_i^{(\alpha,\alpha)}$	$\mathcal{M}_{ij}^{(\alpha,\alpha)}$	$G_{ij,\alpha}$	$H_{ij,\alpha}$	$\frac{\partial \mathcal{M}_{jk}}{\partial x_i}\Big\vert_{\mathbf{x}_\alpha}^{(1)}$	$\mathcal{S}_{i,j}^{(\alpha\beta)}$	$\mathcal{S}_{i,jk}^{(\alpha\beta)}$
Cell-Centered	0	$6N_c$	$9N_c$	$36N_c$	$18N_c$	0	$18N_f$
Vertex-Centered	$3N_v$	$6N_v$	$9N_v$	$36N_v$	$18N_v$	$9N_e$	$18N_e$

4. The *k*-exact projection method

One key element of this work is to combine the presented k-exact reconstruction approach with a fractional step method for the simulation of time-dependent viscous incompressible flows. Fractional step methods, also referred to as projection methods [39], go back to the work of Chorin and Temam [38, 70] and intend to overcome the difficulty of the coupling between pressure and velocity through the incompressibility constraint. Compared to other solution procedures, projection methods require only to solve a single sequence of decoupled equations for the velocity and the pressure at every time step, which makes them very attractive for large scale simulations [39]. Starting point are the Navier-Stokes equations for incompressible

flows, which read

$$\frac{\partial u_i}{\partial x_i} = 0, \tag{63}$$

$$\frac{\partial u_i}{\partial t} + \frac{\partial}{\partial x_j}\left(u_i u_j\right) - \nu \frac{\partial^2 u_i}{\partial x_j^2} = -\frac{1}{\rho_0}\frac{\partial p}{\partial x_i}. \tag{64}$$

A standard incremental pressure-correction scheme [39] is used, which consists of two steps. The first step predicts an interim velocity $\mathbf{u}^*$, which does not satisfy continuity. It is obtained from the initial pressure at time step t_n and taking convective and viscous fluxes into account. The latter are discretized in time using the Crank-Nicolson scheme, which features a second order accuracy in time [41]

$$\frac{u_i^* - u_i^n}{\Delta t} + \frac{1}{2}\frac{\partial}{\partial x_j}\mathcal{F}_{ij}(\mathbf{u}^*) + \frac{1}{2}\frac{\partial}{\partial x_j}\mathcal{F}_{ij}(\mathbf{u}^n) = -\frac{1}{\rho_0}\frac{\partial p^n}{\partial x_i}. \tag{65}$$

The fluxes are calculated according to $\mathcal{F}_{ij}(\mathbf{u}) = u_i u_j^n - \nu(\partial u_i/\partial x_j)$. Note that the convective part uses the velocity u_j^n of time step t_n for both explicit and implicit fluxes, in order to linearize the system of equations. The predictor equations are volume-averaged according to (2), which leads to the following expression

$$\frac{\overline{u}_{i,\alpha}^* - \overline{u}_{i,\alpha}^n}{\Delta t} + \frac{1}{|\Omega_\alpha|}\sum_{\beta\in\mathbb{V}_\alpha^{(1)}}\left[\frac{1}{2}\iint_{A_{\alpha\beta}}\mathcal{F}_{ij}\left(\overline{\mathbf{u}}^*\right)n_j\,\mathrm{d}A + \frac{1}{2}\iint_{A_{\alpha\beta}}\mathcal{F}_{ij}\left(\overline{\mathbf{u}}^n\right)n_j\,\mathrm{d}A\right] = -\frac{1}{\rho_0}\overline{\left(\frac{\partial p^n}{\partial x_i}\right)}_\alpha. \tag{66}$$

It is now possible to apply the introduced k-exact flux-formulations to discretize the surface-integrals and solve for the interim velocity field $\mathbf{u}^*$. However, the volume-averaged pressure gradient on the right hand side differs substantially from the available k-exact gradients at the primary grid nodes, since the latter are point-values at $\mathbf{x}_\alpha$. Thus, an appropriate conversion from point-values to volume-averages is needed to maintain the accuracy. One possibility is to simply use higher derivatives and respective geometric moment tensors, analogous to equation (7). For $k = 2$, this would result in

$$\overline{\left(\frac{\partial p}{\partial x_i}\right)}_\alpha = \left.\frac{\partial p}{\partial x_i}\right|_{\mathbf{x}_\alpha}^{(2)} + \left.\frac{\partial^2 p}{\partial x_i \partial x_j}\right|_{\mathbf{x}_\alpha}^{(1)}\mathcal{M}_j^{(\alpha,\alpha)} + \mathcal{O}\left(h^2\right), \tag{67}$$

whereas for $k = 1$ the volume-averaged pressure gradient coincides with the 1-exact pressure gradient at $\mathbf{x}_\alpha$. Unfortunately, this approach cannot maintain the overall accuracy for a given exactness level. This would require higher derivatives of the pressure at $\mathbf{x}_\alpha$, which is not consistent with the degree of the underlying reconstruction polynomial. We thus propose a method, where a volumetric averaging procedure through a Green-Gauss formulation is applied. For $k = 2$ this leads to the following expression

$$\overline{\left(\frac{\partial p}{\partial x_i}\right)}_\alpha = \frac{1}{|\Omega_\alpha|}\sum_{\beta\in\mathbb{V}_\alpha^{(1)}}\iint_{A_{\alpha\beta}} p\,n_i\,\mathrm{d}A = \frac{1}{|\Omega_\alpha|}\sum_{\beta\in\mathbb{V}_\alpha^{(1)}} p\Big|_{\mathbf{x}_\Gamma}^{(3)}\mathcal{S}_i^{(\alpha\beta)} + \left.\frac{\partial p}{\partial x_j}\right|_{\mathbf{x}_\Gamma}^{(2)}\mathcal{S}_{i,j}^{(\alpha\beta)} + \frac{1}{2}\left.\frac{\partial^2 p}{\partial x_j \partial x_k}\right|_{\mathbf{x}_\Gamma}^{(1)}\mathcal{S}_{i,jk}^{(\alpha\beta)} + \mathcal{O}\left(h^3\right). \tag{68}$$

The face values of p at $\mathbf{x}_\Gamma$ and its derivatives are approximated as central averages from the reconstructed face-values of the two adjacent elements Ω_α and Ω_β. In this way the desired order of accuracy is preserved. Both approaches will be tested by means of benchmark simulations in the following section.

Once the interim velocity field $\mathbf{u}^*$ has been determined, it is used to estimate the final velocity at t_{n+1}

using the projection step

$$\frac{u_i^{n+1} - u_i^*}{\Delta t} = -\frac{1}{\rho_0}\left(\frac{\partial p^{n+1}}{\partial x_i} - \frac{\partial p^n}{\partial x_i}\right). \tag{69}$$

The unknown pressure gradient at t_{n+1} is calculated by solving a Poisson equation, which is obtained from the divergence of the momentum equations (64) and under consideration of the continuity equation (63)

$$\frac{\partial}{\partial x_i}\left(\frac{\partial p^{n+1}}{\partial x_i}\right) = \frac{\rho_0}{\Delta t}\frac{\partial u_i^*}{\partial x_i} + \frac{\partial}{\partial x_i}\left(\frac{\partial p^n}{\partial x_i}\right). \tag{70}$$

Similar to the predictor step, this equation is discretized in space according to

$$\sum_{\beta\in\mathbb{V}_\alpha^{(1)}} \iint_{A_{\alpha\beta}} \left(\frac{\partial p^{n+1}}{\partial x_i}\right) n_i \,\mathrm{d}A = \sum_{\beta\in\mathbb{V}_\alpha^{(1)}} \left[\frac{\rho_0}{\Delta t}\iint_{A_{\alpha\beta}} u_i^* n_i \,\mathrm{d}A + \iint_{A_{\alpha\beta}} \left(\frac{\partial p^n}{\partial x_i}\right) n_i \,\mathrm{d}A\right]. \tag{71}$$

The integrals comprising the pressure gradients are approximated by using the k-exact diffusive flux formulation, which has been presented in equation (57). The surface-integral on the right hand side involving the interim velocity field is approximated according to

$$\iint_{A_{\alpha\beta}} u_i^*\, n_i \,\mathrm{d}A = \dot{m}^* \Big|_{\mathbf{x}_\Gamma}^{(k+1)} + |A_{\alpha\beta}|\,\mathcal{O}\left(h^{k+1}\right). \tag{72}$$

where the mass flux term $\dot{m}^*|_{\mathbf{x}_\Gamma}^{(k+1)}$ from equation (46a) is formed with u_i^*. For collocated arrangements of pressure and velocity, spurious oscillations may occur as the pressure gradient calculation is based on central averages [41]. Typically, a stabilization term based on the work of Rhie and Chow [71] is added to the interpolated face velocities $\mathbf{u}^*$ to prevent a decoupling of the pressure and the velocity field [41]. This term introduces an error of $\mathcal{O}(h^3)$ on cartesian grids [72], but can lead to more severe errors when grids tend to be distorted. However, for all the grids used in this work it was found that the presented k-exact multiple correction approach does not require an auxiliary Rhie-Chow stabilization term to prevent spurious pressure oscillations. We believe this is due to the fact, that larger stencils are used for the calculation of the volume-averaged pressure gradient and for the discretized divergence of the interim velocity field $\partial u_i^*/\partial x_i$. This leads to a stronger coupling between pressure and velocity field and thus prevents the solution from odd-even decoupling. Once the new pressure field is obtained, it is used to correct the interim velocity $\mathbf{u}^*$. For consistency, equation (69) must also be volume-averaged to preserve the k-exactness

$$\overline{u}_{i,\alpha}^{n+1} = \overline{u}_{i,\alpha}^{n} - \frac{\Delta t}{\rho_0}\left[\overline{\left(\frac{\partial p^{n+1}}{\partial x_i}\right)}_\alpha - \overline{\left(\frac{\partial p^n}{\partial x_i}\right)}_\alpha\right]. \tag{73}$$

The averaged pressure gradients must be calculated using one of the methods already described. The required operations to perform a 2-exact projection step are summarized in Algorithm 2.

Algorithm 2 Procedure to perform the 2-exact projection step

procedure DO PROJECTION($\overline{\mathbf{u}}^n, \overline{p}^n$)
  for $\alpha \leftarrow 1$ to N **do**
    Perform a 2-exact reconstruction of $\overline{\mathbf{u}}^n$ and $\overline{p}^n$ on Ω_α according to algorithm (1)
    Compute the volume-averaged pressure gradient $\overline{\left(\frac{\partial p}{\partial x_i}\right)}_\alpha^n$ using (67) or (68)
  for $A_{\alpha\beta} \leftarrow \Omega_\alpha \cap \Omega_\beta, \quad \Omega_\alpha, \Omega_\beta \in \mathcal{D}(\Omega)$ **do**
    Compute massflux-tensors $\dot{m}$ (46a)-(46c) and store them at the element interface $A_{\alpha\beta}$
  Solve the volume-averaged momentum predictor step (65) for $\overline{\mathbf{u}}^*$
  for $\alpha \leftarrow 1$ to N **do**
    Perform a 2-exact reconstruction of $\overline{\mathbf{u}}^*$ on Ω_α according to algorithm (1)
  Solve the volume-averaged Poisson equation (71) for new pressure field $\overline{p}^{n+1}$
  for $\alpha \leftarrow 1$ to N **do**
    Compute the volume-averaged pressure gradient $\overline{\left(\frac{\partial p}{\partial x_i}\right)}_\alpha^{n+1}$ using (67) or (68)
    Obtain the divergence-free velocity field $\overline{\mathbf{u}}_\alpha^{n+1}$ (73)

5. Numerical benchmarks

This section is devoted to the validation of the accuracy and the performance properties of the proposed 1- and 2-exact multiple-correction schemes. The schemes have been implemented into ThetaCOM, which is developed at the DLR Institute of Combustion Technology. ThetaCOM has been extensively used for the simulation of incompressible and variable density flow problems, for example, detailed large-eddy simulations of complex combustion applications [42, 43, 44, 45, 46, 47, 48, 49]. The solver uses a collocated, edge-based representation with median-dual cells that are constructed from hybrid primary grid elements, such as tetrahedra, hexahedra, pyramids or prisms. The Poisson equation for the pressure is solved using the preconditioned flexible generalized minimal residual method (GMRES). As preconditioning a single multigrid V cycle is used on three grid levels. The k-exact multiple-correction is only employed on the finest grid level. All other transport equations are solved using a biconjugate gradient stabilized method (BiCGSTAB) with Jacobi preconditioning. All linear equations are formulated in a matrix-free approach, which reduces the memory requirements significantly by avoiding additional storage for sparse matrix data structures.

The 1- and 2-exact multiple-correction is tested against conventional methods already implemented in ThetaCOM. Here, convective fluxes are either discretized with a central differencing scheme (referred to as CDS), or with the low-dissipation low-dispersion scheme by Loewe et al. [66, 73] (referred to as $LD2$). The respective flux-coefficients are given in Table 1. For both these conventional schemes, diffusive fluxes are discretized with the original Mathur-Murthy formulation in equation (58). In contrast, the additional terms (59) and (60) are only used for the 1- and 2-exact schemes, respectively. For all test cases, a Crank-Nicolson scheme is used for the temporal discretization, as proposed for the predictor step of the momentum Equations (66). The latter features a second order accuracy in time. Besides this, small Courant-Friedrichs-Lewy (CFL) numbers are used to ensure that the temporal errror does not affect the results and the convergence history. All implicit fluxes are calculated with a deferred-correction procedure according to Khosla and Rubin [74]. Thus derivatives used for the reconstruction are only updated once at the end of every time step. This results in a splitting of the explicit and implicit flux parts which is formally not purely central in the sense of the Crank-Nicolson scheme. However, numerical experiments showed that this approach significantly increases the overall performance of all schemes, since the calculation of gradients accounts for a major part of the overall computation time during one time step. At the same time, it was

also found that the resulting error from this deferred-correction approach is negligible. For both the k-exact schemes, the proposed projection method is utilized, which does not rely on any additional stabilization techniques for the pressure-velocity coupling. Both the conventional discretization methods employ an incremental variant of the projection method as described by Knopp et al. [75], where the interpolation scheme by Rhie and Chow [71] is used to avoid spurious pressure oscillations.

In the following sections, the influence of the proposed k-exact scheme on the accuracy of diffusive and convective fluxes will be emphasized through canonical test cases, namely the linear diffusion of an instantaneous point source and the convection of a vortex in a uniform flow field. Additionally, the lid driven cavity problem and the laminar flow around a cylinder in $2D$ will be considered, in order to show the scheme's capability to enhance the solution of time dependent viscous flows in the presence of Dirichlet boundary conditions. Finally, a benchmark for the laminar flow around a sphere will be performed, where it is shown that the present approach can be applied to the simulation of fully three-dimensional flows.

5.1. Linear diffusion of an instantaneous point source

This first test case aims to show the superior properties of the introduced k-exact discretization of the diffusive fluxes. This is achieved by solving the general transport equation (1) under consideration of a non-moving flow field with $\mathbf{u} = \mathbf{0}$ and in the absence of any sinks or sources. The problem is set up in a two dimensional domain $\mathbf{x} \in [-L, L]^2$ and the diffusion coefficient D is set constant. An initial concentration of ϕ is released locally in the center of the domain $\mathbf{x}_0 = [0, 0]^{\mathrm{T}}$ by means of a Dirac pulse $\phi(\mathbf{x}, t = 0) = \delta(\mathbf{x})$. Assuming the domain to be sufficiently large, the temporal evolution of the passive scalar can be calculated analytically with

$$\phi(\mathbf{x}, t) = \frac{1}{4\pi D t} \exp\left[-\frac{(x - x_0)^2 + (y - y_0)^2}{4Dt}\right]. \tag{74}$$

The domain is initialized with the concentration of $\phi(\mathbf{x}, t_0)$ at a specified time $t_0 = 0.25\,\mathrm{s}$ and the passive scalar decays for a simulation time of one second. The final concentration is compared to the analytic solution at $t_1 = 1.25\,\mathrm{s}$. The reference length is set to $L = 1\,\mathrm{m}$ and a diffusion coefficient $D = 0.005\,\mathrm{m}^2/\mathrm{s}$ is chosen, so that all boundaries of the domain are located sufficiently far away from the center. Four meshes are analyzed, whose primary representation consist of randomly distorted triangles. Since the employed solver can handle only three-dimensional elements, the meshes actually consist of prismatic elements. The third coordinate direction is neglected and symmetry boundaries are applied. A representative mesh with $N = 32^2$ primary grid nodes is presented in Figure 4. The grids are created by randomly shifting $N \times N$ primary grid nodes within the domain, which is followed by a Delaunay triangulation. The diffusive fluxes are either approximated through the proposed 2-exact approach, a 1-exact approach or the original Mathur and Murthy formulation, as given in equation (57). The accuracy of the numerical schemes is analyzed with the L_2-norm

$$E_{L_2}(\phi) = \left[\frac{\sum_{\alpha=1}^{N} \left(\overline{\phi}_\alpha - \overline{\phi}_\alpha^{\mathrm{ex}}\right)^2 |\Omega_\alpha|}{\sum_{\alpha=1}^{N} |\Omega_\alpha|}\right]^{1/2} \tag{75}$$

with the volume-averaged exact solution $\overline{\phi}_\alpha^{\mathrm{ex}}$ and the total number of elements N. The latter is successively increased from $N = 16^2$ to $N = 128^2$. Figure 5 displays the resulting L_2-norm errors of the benchmark. The 0-exact flux approximation, which refers to the original Mathur and Murthy formulation, only converges to a first order of accuracy due to the grid deformation. This error can be attributed to the deviation between primary grid nodes and element centroids. It is corrected in the 1-exact scheme by the term $F_{D,EX1}^{(\alpha\beta)}$ in equation (57), which leads to a second-order accurate solution. Due to the reasons mentioned in Section 3.2, the 2-exact diffusive flux formulation converges only with $\mathcal{O}\left(h^2\right)$ and features slightly smaller errors than the 1-exact formulation. It thus seems, that the second correction term $F_{D,EX2}^{(\alpha\beta)}$ in equation (57) has only minor effects on the overall accuracy.

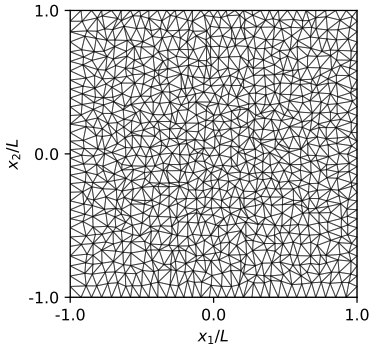

Figure 4: Mesh for the $2D$ linear diffusion benchmark with $N = 32^2$ primary grid nodes.

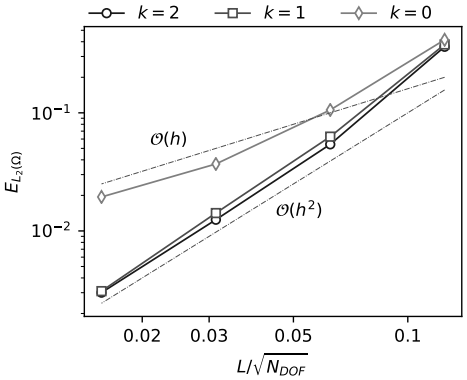

Figure 5: Grid convergence of the L_2-error norm for the $2D$ linear diffusion benchmark. k refers to the exactness of the underlying approximation for diffusive fluxes.

5.2. Convection of a vortex on a periodic grid

The next test case describes the convection of a $2D$ vortex in an inviscid, incompressible and uniform flow field. It intends to show the superior capabilities of the k-exact schemes to capture the convective transport. The vortex is defined by the velocity and pressure fields

$$u_1(\mathbf{x}, t = 0) = u_\infty + \frac{\partial \psi}{\partial x_2} \qquad \text{and} \qquad u_2(\mathbf{x}, t = 0) = -\frac{\partial \psi}{\partial x_1}, \tag{76a}$$

$$p(\mathbf{x}, t = 0) = p_\infty - \frac{1}{2}\rho \left(\frac{\Gamma}{\sigma}\right)^2 \exp\left[-\frac{(x_1 - x_{1,c})^2 + (x_2 - x_{2,c})^2}{\sigma^2}\right], \tag{76b}$$

with a free-stream velocity u_∞ in x_1 direction and an ambient pressure p_∞. The field variables are deduced from the stream function ψ

$$\psi(\mathbf{x}, t = 0) = \Gamma \exp\left[-\frac{(x_1 - x_{1,c})^2 + (x_2 - x_{2,c})^2}{2\sigma^2}\right] \tag{77}$$

with circulation Γ, vortex radius σ and vortex center $\mathbf{x}_c$. The exact solution to the problem is simply the convection of the vortex at free-stream velocity. Thus its shape must be preserved as accurately as possible by the underlying numerical scheme. The numerical solution to the problem is obtained from the discretized Navier-Stokes equations (63) and (64) with vanishing viscosity $\nu = 0$. Additionally, the convection of a passive scalar ϕ with the vortex is investigated. The initial concentration ϕ is given by

$$\phi(\mathbf{x}, t = 0) = A \exp\left[-\frac{(x_1 - x_{1,c})^2 + (x_2 - x_{2,c})^2}{\sigma^2}\right], \tag{78}$$

such that it features the same extend as the vortex and therefore must also be preserved in its shape. A periodic domain $\mathbf{x} \in [0, L]^2$ is employed and a grid convergence study is performed for a convection distance of $\delta x = L$, which intends to estimate the actual orders of magnitude by which the numerical error decreases. The chosen parameters are given in Table 3. The meshes are generated in the same manner as for the linear diffusion benchmark, shown in Figure 4. The convergence of the numerical schemes is examined by successively increasing the number of elements in the domain from $N = 32^2$ to $N = 256^2$. A CFL number of 0.1 is set for all simulations. It has been demonstrated in a separate convergence study of the numerical

time step that with this value for the CFL number the influence of temporal discretization errors can be neglected.

Table 3: Parameters used for the vortex convection test case.

Parameter	L	u_∞	p_∞	ρ	σ	$x_{1,c}$	$x_{2,c}$	Γ	A
Value	0.1 m	20 m/s	100,000 Pa	1.0 kg/m^3	0.005 m	0.05 m	0.05 m	0.4 m^2/s	0.4

Figure 6 shows the grid convergence for both x_1-velocity and pressure, calculated with the k-exact multiple correction method for $k = 1$ and $k = 2$. The simulations have been performed with both variations of the volume-averaged pressure gradient, which is needed for the right hand side of the momentum predictor and for the correction of the interim velocity field. The approach described by equation (67) is denoted as Type 1, whereas for Type 2 the gradient is calculated according to equation (68). Both formulations do not show any significant difference when the 1-exact discretization is chosen. In contrast, the 2-exact multiple-correction method produces significantly higher errors when using the Type 1 formulation. This is to be expected, since this procedure formally approximates the averaged pressure gradient only with $\mathcal{O}(h^2)$. Interestingly, this error has a greater effect on the calculation of the velocity field than on the pressure. Due to the enhanced accuracy, the volume-averaged pressure gradient will be calculated according to the Type 2 formulation in all of the following simulations, as the 2-exact reconstruction is used. The Type 1 gradient is used for the 1-exact approach, since this formulation has proven to be more stable for the upcoming test cases.

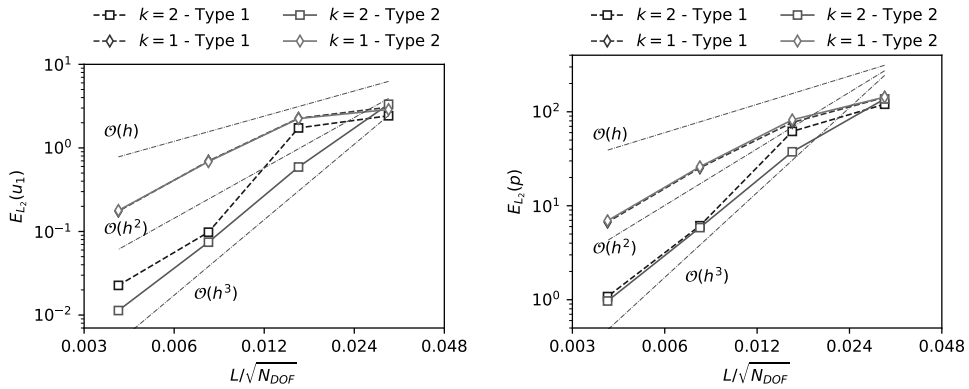

(a) L_2-error of velocity u_1

(b) L_2-error of pressure p

Figure 6: Grid convergence for the $2D$ vortex convection on a periodic grid regarding the discretization of the averaged pressure gradient. k refers to the employed exactness level for the convective flux discretization. Type 1 refers to the averaged pressure calculated with equation (67), whereas for Type 2 equation (68) has been used.

The performance of the different discretization schemes is assessed by comparing the average iteration time τ_{it} estimated for every simulation. It is normalized with the highest average iteration time $\tau_{it,max}$ achieved in all simulations. Simulations are carried out for both 1- and 2-exact schemes, as well as the conventional $LD2$ and CDS schemes, described above. Due to the iterative solution procedure for the pressure equation, the 2-exact approach requires a continuous update for both gradient and Hessian matrix in every sub-iteration, which significantly increases the computation time. Hence, it is further examined how the numerical error behaves, when different exactness levels are employed for pressure and momentum. A promising approach is to apply the 2-exact reconstruction for momentum fluxes in equation (66) and the discretized divergence of the interim velocities u_i^* in the pressure equation (71). On the other hand, the

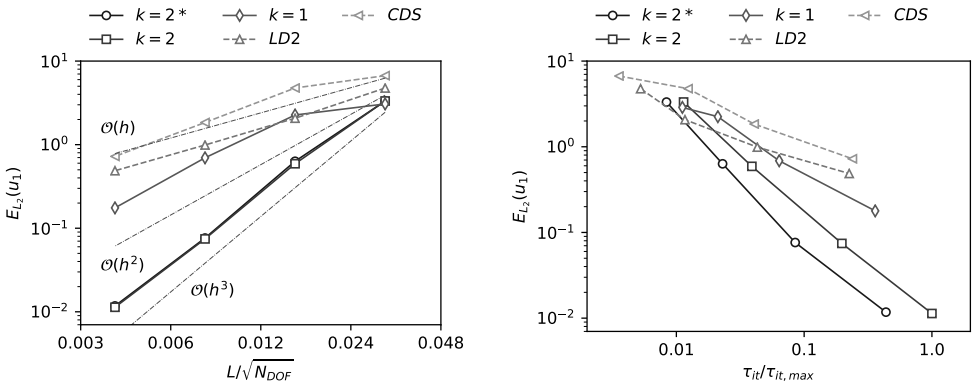

(a) L_2-error of velocity u_1

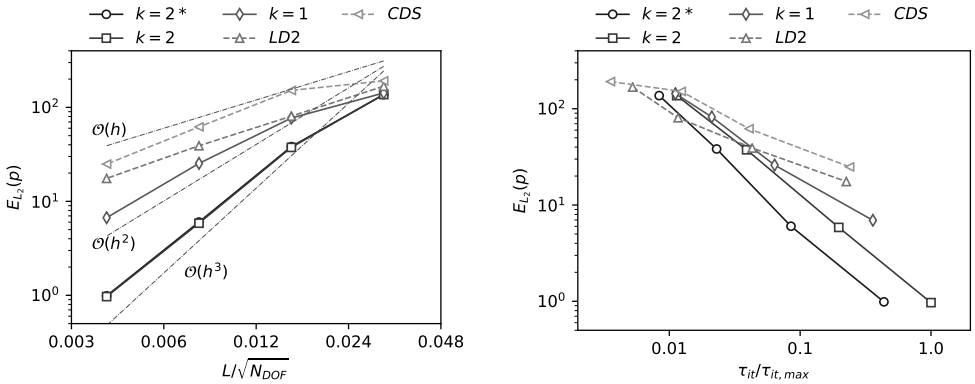

(b) L_2-error of pressure p

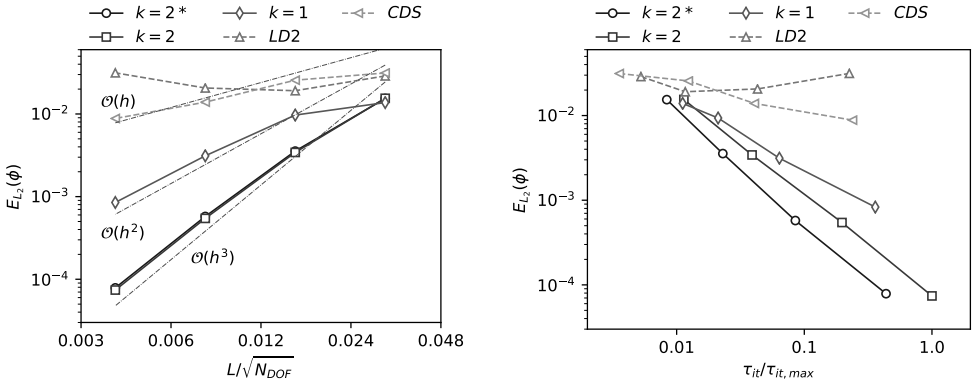

(c) L_2-error of passive scalar ϕ

Figure 7: Grid convergence and performance regarding the $2D$ vortex convection on a periodic grid. k refers to the employed exactness level for the convective flux discretization. For $k = 2^*$, velocities are reconstructed with $k = 2$ and the pressure with $k = 1$.

fluxes involving the pressure in equation (71) are treated with the 1-exact approach, thus the Hessian matrix for the pressure no longer needs to be updated in every sub-iteration. This scheme will be referred to as

2^*-exact. Figures 7a to 7c show the resulting L_2-norm errors obtained for velocity in x_1 direction, pressure and the passive scalar. The 1- and 2-exact schemes preserve the prescribed accuracy levels, especially for the convection of the passive scalar. On the contrary, both conventional schemes only reach a first order of accuracy due to the strong deformation of the employed grids. The $LD2$-scheme even fails to accurately predict the convection of the passive scalar. There is a slight deviation from $\mathcal{O}(h^3)$ in the pressure for both 2- and 2^*-exact schemes on the left in Figure 7b. This is due to the fact that the 2-exact pressure fluxes in equation (71) only preserve an accuracy of $\mathcal{O}(h^2)$, even if both correction terms are utilized. Since the overall convergence is higher than $\mathcal{O}(h^2)$, we suggest that that the divergence of the interim velocity field $\partial u_i^*/\partial x_i$ on the right hand side of the pressure equation is the leading contributor to the numerical error and thus should be discretized with higher orders of accuracy in general.

Concerning the performance, both 2-exact schemes require significantly less time to predict the solution for a desired error threshold than the conventional schemes. For example, the 2^*-exact method requires only a tenth of the time compared to the CDS-scheme to fall below an error accuracy of $E_{L_2}(u_1) \leq 7 \times 10^{-1}$ for the u_1-velocity, as a significantly coarser grid can be used. The performance increase is particularly apparent for the convection of the passive scalar, shown on the right of Figure 7c. The solution obtained from both 2-exact schemes on a grid with $N = 32^2$ elements clearly outperforms the solution obtained from both conventional schemes on the finest grid resolution with $N = 128^2$ elements. Comparing both 2-exact schemes, the 2^*-exact method is approximately twice as fast in the calculation of a single time step for a fixed number of elements. This is due to the fact, that the Hessian matrix of the pressure must not be updated in every single sub-iteration. Since this approach does not noticeably affect the numerical error, the 2^*-exact scheme will be used for all upcoming benchmark simulations.

5.3. Convection of a vortex on an expanding grid

The vortex convection is now performed for a larger distance and for a mesh that consists of expanding elements. This gives the opportunity to further analyze the influence of a deformed mesh on the preservation of the vortex structure. A domain of size $\mathbf{x} \in [0, 10L] \times [0, L]$ is considered, with a convection distance of $\delta x = 9L$. The same parameters for the vortex are chosen as for the previous test case, given in Table 3. A single simulation is performed for all discretization schemes on a mesh with 1280 primary grid nodes in x_1-direction and 256 nodes in x_2-direction. The grid is the resulting Delaunay triangulation of a set of nodes that are displaced to a small extent and whose spacing increases in x_1-direction. A similar grid is shown in Figure 8, where the resolution has been reduced for reasons of clarity. Figures 9a to 9c show the numerical solution obtained for $\overline{u}_{1,\alpha}$, $\overline{p}_\alpha$ and $\overline{\phi}_\alpha$ after a convection of $\delta x = 9L$. The black contours highlight the analytic solution, according to which the minimum and maximum values are given in the respective colorbars. The 2^*-exact scheme preserves the shape and absolute values of the vortex and the passive scalar very well. This proves its superior dispersion and dissipation properties, even on highly distorted grids. For the 1-exact reconstruction the overall shape of vortex and passive scalar is deformed and the structure is shifted from the actual center. The solution also deviates from the analytic values in terms of absolute values, which reveals the inferior dispersion properties in contrast to the 2^*-exact method. These effects are even more apparent for both the $LD2$- and CDS-discretization. Particularly the solution of the conventional CDS-scheme is influenced by a strong dispersive error. For $LD2$ the preservation of the vortex shape and position is slightly enhanced compared to the CDS-method. However, it is clearly not able to preserve the shape of the convected passive scalar.

5.4. Lid driven cavity problem at $Re = 1000$

The lid driven cavity problem is a well-known benchmark for incompressible flow solvers [37, 76, 77, 78, 79, 80] and it is considered here to evaluate the k-exact discretization approach under the influence of Dirichlet boundary conditions. A cavity of size $\mathbf{x} \in [0, L]^2$ is taken into account, with a reference length $L = 1\,\mathrm{m}$. The top of the cavity is a moving lid with velocity $u_1 = 1.0\,\mathrm{m/s}$ and $u_2 = 0.0\,\mathrm{m/s}$, whereas the three remaining boundaries are no-slip walls with $u_1 = u_2 = 0.0\,\mathrm{m/s}$. Simulations are performed on three meshes with $N = \{32^2, 64^2, 128^2\}$ primary grid nodes as depicted in Figure 10. All grids consists of elements with maximum aspect ratios of approximately 15. A CFL number of 0.2 has been chosen, such

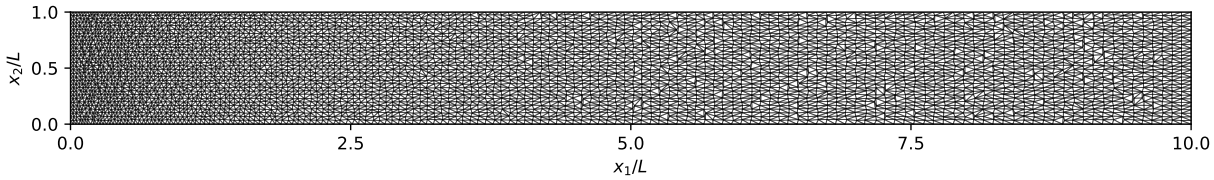

Figure 8: Expanding grid for the vortex convection. The shown grid features a reduced resolution for clarity reasons.

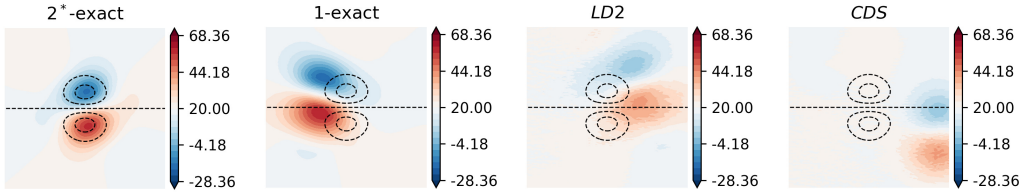

(a) Volume-averaged velocity $\overline{u}_{1,\alpha}$ in m/s

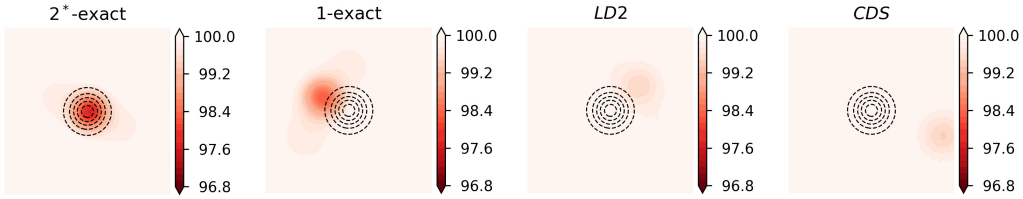

(b) Volume-averaged pressure $\overline{p}_{\alpha}$ in kPa

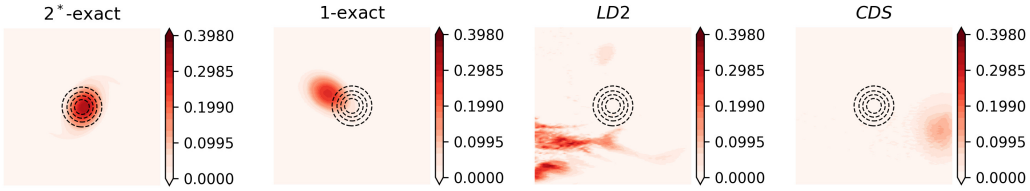

(c) Volume-averaged passive scalar $\overline{\phi}_{\alpha}$

Figure 9: Benchmark results for the vortex convection on an expanding grid, obtained for a convection distance of $\delta x = 9L$ with various discretization schemes. Black contours indicate the analytical solution.

that the influence of the temporal discretization error can be neglected. To ensure a converged solution, the simulations are run until the change of the kinetic energy E_k in the entire domain between two succeeding time steps varies less than $|E_k^{n+1} - E_k^n| < 10^{-6}\,\mathrm{m}^2/\mathrm{s}^2$.

Figure 11a shows the stream function ψ in the domain, calculated for both k-exact schemes on the finest mesh with $N = 128^2$ nodes. The stream function ψ is estimated by taking the divergence of the following

equation

$$\frac{\partial \psi}{\partial x_1} + \frac{\partial \psi}{\partial x_2} = u_1 - u_2 \tag{79}$$

and solving it similarly to the Poisson equation of the pressure correction with the underlying flow field $\mathbf{u}$. Both results agree well with simulations in several works that are highly referenced for this benchmark, such as Ghia et al. [78], Botella and Peyret [76] or Bruneau and Saad [77]. The flow field is characterized by a dominant vortex in the center of the domain and two smaller vortices in both lower corners of the cavity. Figure 12 shows velocity profiles for u_1 and u_2 calculated with both k-exact schemes on all three meshes. These are compared to results given by Ghia et al. [78]. In both cases, even the profiles on the coarse grid agree remarkably well to the reference values. There are no visual differences between the reference data and the solutions obtained with the finer grids. Similar results have been obtained for both the conventional $LD2$ and CDS schemes, which are therefore not shown. The choice of the discretization scheme has a larger influence on the calculation of the primary vortex, which is determined by local minima of the stream function ψ. Table 4 shows calculated point values for the stream function minimum in the cavities primary vortex, estimated with different discretization schemes on the mesh with $N = 64^2$ nodes. Additionally, the associated vorticity ω and the respective vertex center coordinates are given. The 2*-exact scheme features for both ψ and ω the greatest agreement to the reference values, followed by the 1-exact scheme. Also the x_1-coordinate of the vortex center agrees well in both cases, whereas the x_2 coordinate differs slightly. However, these coordinates must be taken with caution, as they only correspond to the coordinates of the primary grid nodes at which the local minimum of ψ was determined.

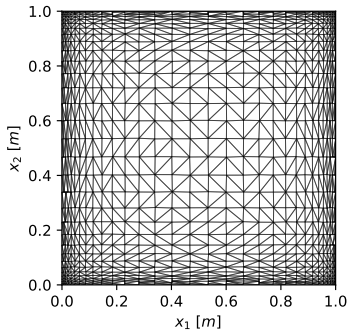

Figure 10: Lid driven cavity problem grid with $N = 32^2$ primary grid nodes.

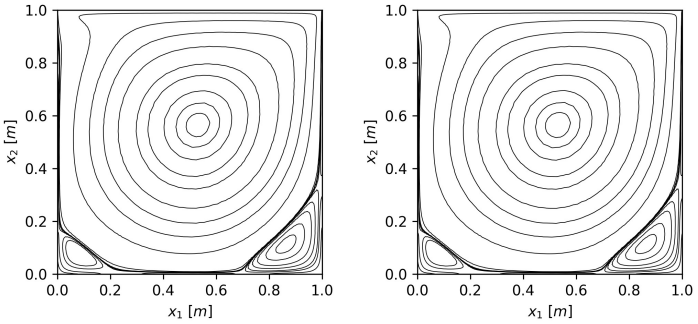

(a) 2*-exact scheme (b) 1-exact scheme

Figure 11: Contours for stream function ψ for the lid driven cavity at $Re = 1000$ for $N = 128^2$.

Table 4: Comparison on the primary vortex quantities of the lid driven cavity problem with $Re = 1000$.

	N	ψ [m^2/s]	ω [1/s]	x_1 [m]	x_2 [m]
Botella and Peyret [76]	160 (spectral)	−0.118937	2.06775	0.54308	0.56520
Bruneau and Saad [77]	128 × 128	−0.118920	2.06740	0.53125	0.56543
2*-exact	64 × 64	−0.118760	2.07987	0.54927	0.58171
1-exact	64 × 64	−0.118710	2.03657	0.54927	0.58171
$LD2$	64 × 64	−0.117377	2.01889	0.51698	0.54930
CDS	64 × 64	−0.118263	2.04903	0.51698	0.54930

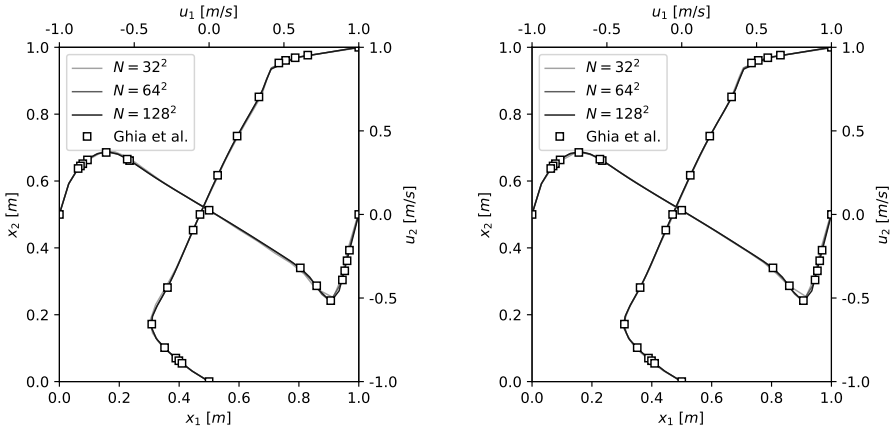

(a) 2^*-exact scheme

(b) 1-exact scheme

Figure 12: Velocity-profiles for the lid driven cavity benchmark at $Re = 1000$ obtained with the k-exact reconstruction approach. The profiles are linearly interpolated from point-values of u_1 and u_2. Reference values are taken from Ghia et al. [78]

5.5. Laminar flow around cylinder in 2D

This benchmark was proposed by Schaefer et al. [81] within the DFG high priority research program *Flow Simulation with High-Performance Computers*. It has been used by several authors to demonstrate the capability of high-order schemes to accurately predict time-dependent, viscous flows [37, 79, 80]. Simulations are performed for the flow around a circular cylinder at $Re = 100$. A cylinder of diameter 0.1 m is placed in a channel of dimension $2.2\,\mathrm{m} \times 0.41\,\mathrm{m}$. No-slip walls are employed for the top and bottom boundary conditions of the channel and a parabolic inflow velocity profile is applied at the inlet. For details concerning the setup we refer to the test case $2D$-2 in [81]. At the specified Reynolds number, a Karman vortex street forms behind the cylinder, leading to periodic oscillations of the drag and lift forces that exert on it. The maximum drag and lift coefficients, as well as the resulting Strouhal number from the periodic oscillations are used to evaluate the solution. Four meshes are considered with an increasing number of primary grid nodes $N = \{4920, 10390, 19790, 39622\}$. The grids consist of prismatic elements in the core region of the channel and hexahedral layers in the vicinity of no-slip walls. Thus, the curved cylinder surface is approximated by planar quadrilaterals and elements near the cylinder were refined to keep the corresponding error due to curvature sufficiently small. Similar to the previous benchmarks, the x_3-coordinate direction is neglegted, which is accounted for by using symmetry boundary conditions. Figure 13 shows the coarsest mesh with 4920 primary grid nodes. The simulations are performed with all four discretization schemes for a total simulation time of 10 s and with a time step $\Delta t = 10^{-4}\,\mathrm{s}$.

Figure 14 displays the solution at a state, where the lift force becomes largest. The solution has been obtained with the 2^*-exact scheme for the meshes with $N = 10390$ and $N = 39622$ nodes. In both cases the Karman vortex street is clearly visible and the results are in very good agreement to those given in other works which utilized high-order methods for this benchmark [37, 79, 80]. Even on the coarse mesh the absolute values for all quantities are predicted accurately. Figure 15 displays a selection of the temporal history of the lift and drag coefficient C_D and C_L, calculated on the coarse mesh with $N = 10390$ and with both k-exact methods. The temporal patterns for both coefficients agree well with data provided in literature [37, 79, 80]. It also highlights a distinct phase shift in both coefficients as the order of accuracy is increased. The latter is less an indication of accuracy, but suggests that the shedding process is triggered slightly differently by the schemes. A similar behavior was also obtained in the work of Bassi et al. [37], who employed a discontinuous Galerkin method for incompressible flows with an artificial compressibility

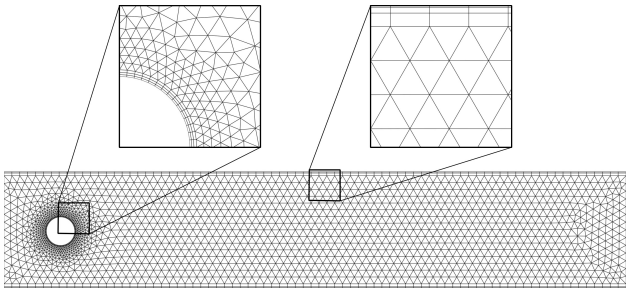

Figure 13: Mesh with $N = 4920$ primary grid nodes, which is used for the laminar flow around a cylinder benchmark.

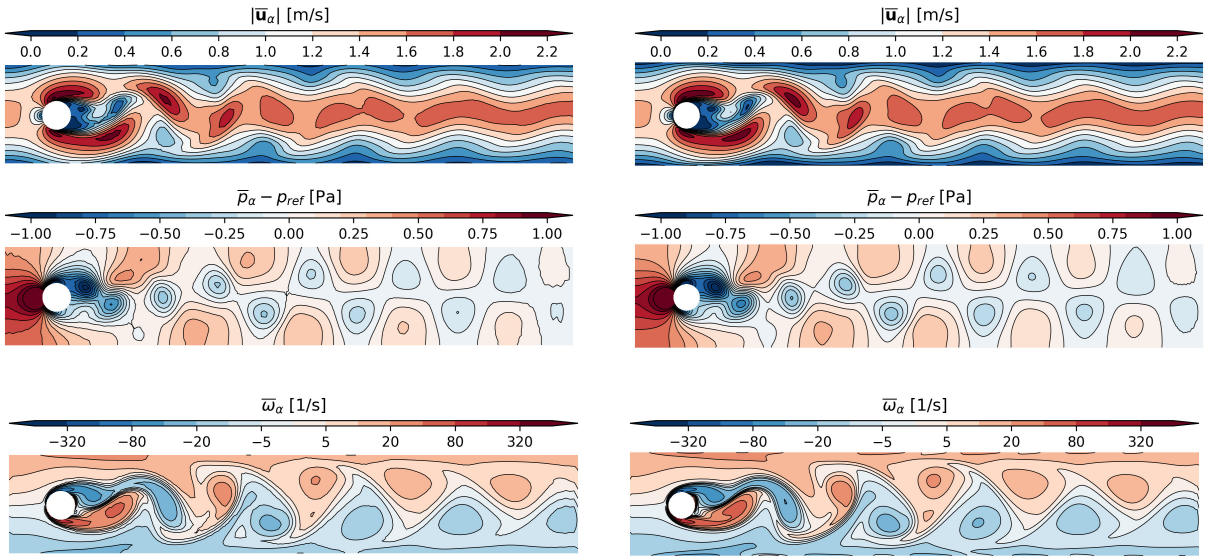

(a) $N = 10390$ (b) $N = 39622$

Figure 14: Solution for the laminar flow around a cylinder in $2D$ at a state of maximum lift force simulated with the 2*-exact scheme. Displayed are absolute velocities (top), the pressure difference to a reference pressure p_{ref} (middle) and the vorticity (bottom).

approach. A quantitative comparison of the present results is given in terms of a grid convergence study for the maximum drag and lift coefficients, $C_{D,max}$ and $C_{L,max}$, as well as the Strouhal number $St = (Df)/U$. The latter is calculated from the cylinder diameter $D = 0.1\,\mathrm{m}$, the mean velocity $U = 1.0\,\mathrm{m/s}$ and the estimated frequency of the lift coefficient f. The resulting values are determined on the basis of simulations for the described discretization schemes and are displayed in Figure 16. They are compared against reference bounds provided by Schaefer et al. [81], which are highlighted by means of dashed areas. The performance of the schemes is analyzed through the average iteration time τ_{it}, which is normalized with the maximum iteration time $\tau_{it,max}$ of all simulations. Remarkably, the Strouhal number has been predicted accurately by all simulations within the given bounds. However, there are large discrepancies in the prediction of both maximum drag and lift coefficients when the conventional discretization schemes are employed. Even on the finest mesh, both techniques fail to accurately predict the value of $C_{L,max}$. Contrary, the values for $C_{D,max}$ and $C_{L,max}$ are calculated accurately even with a coarse mesh of $N = 10390$ nodes when using both 1- and 2*-exact methods. As a result, the average iteration time is significantly reduced when using these schemes to calculate the coefficients within the prescribed ranges. Considering $C_{D,max}$, the 2*-exact scheme requires

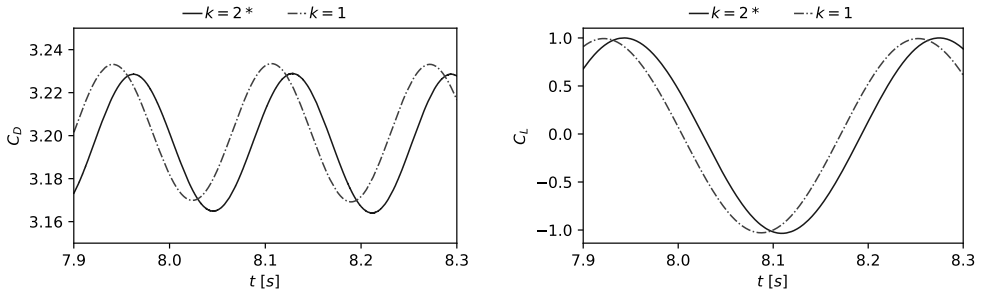

Figure 15: Time histories of a single period for drag coefficient C_D (left) and lift coefficient C_L (right) for the laminar flow around a cylinder in $2D$, obtained with the 1- and 2^*-exact reconstruction approach and for $N = 10390$.

$N = 4920$ and the 1-exact scheme $N = 10390$ elements for an accurate prediction. It thus can be stated, that both methods roughly require only 20% of the simulation time, that would be required to calculate the same result with the $LD2$-scheme. For $C_{L,max}$, both k-exact schemes give accurate predictions for $N = 10390$. Thus, the 1-exact scheme takes slightly less time to predict a desired level of accuracy in this case. If the computation time is considered for a fixed number of degrees of freedom, the 2^*-exact method exceeds the mean iteration of the conventional schemes by a factor of approximately 1.5 to 2.0. For the 1-exact method this factor is in the range of 1.0 to 1.5 and in both cases it increases as the mesh is refined. All in all, it is clearly shown that both proposed schemes are capable of giving accurate predictions on the coarser grids and thus enhancing the overall performance.

5.6. Laminar flow around a sphere in 3D

This benchmark serves to show the ability of the proposed k-exact discretization approach to enhance three-dimensional, time-dependent, viscous flow simulations on fully unstructured grids. A sphere with radius $r = 1\,\text{mm}$ is considered, which is placed in a domain of size $120\,\text{mm} \times 30\,\text{mm} \times 30\,\text{mm}$. To obtain a desired Reynolds number of $Re = 300$, an inflow velocity $u_1 = 1.5\,\text{m/s}$ is imposed and the kinematic viscosity is set to $\nu = 10^{-5}\,\text{Pa s}$. For this Reynolds number, the flow is characterized by a shedding of vortices, which have the structure of symmetrical hairpins [82]. For the surface of the sphere a no-slip wall boundary condition is applied. To study the influence of the grid resolution on the accuracy of the solution, three grids of different element sizes are employed, comprising $N = \{139589, 252101, 610159\}$ primary grid nodes. The grids predominantly consist of tetrahedral elements. Elements are refined in the vicinity of the sphere to a mean size from 0.2 mm to 0.5 mm, in order to reduce the error of the curved boundary approximation through planar surface elements. Prismatic elements are used for the boundary layer, with a mean element size from 0.04 mm to 0.08 mm and the first layer height from 0.004 mm to 0.010 mm. The element size in the wake of the sphere ranges from 0.3 mm to 0.75 mm. Figure 17 shows a cross-section of the coarsest grid. A time step of $7 \times 10^{-6}\,\text{s}$ has been used for all simulations, in order to maintain $CFL < 0.5$ on all grids. Similarly to the two-dimensional flow around a cylinder, the temporal evolution of the drag and the lateral force coefficient C_D and C_D are calculated from the forces exerting on the sphere. The lateral component is defined as the force acting in the direction of the symmetry plane of the wakes vortical structures. The simulation quality is assessed by mean values of lateral force and drag coefficients, their oscillation amplitudes and the resulting Strouhal number.

Figure 18 shows two oscillation periods of both the drag coefficient C_D and lateral force coefficient C_L calculated with the k-exact schemes on the finest grid. Both schemes predict similar temporal histories for the lateral force coefficient, whereas the drag mean coefficient is slightly reduced as the 2^*-exact scheme is employed. Irrespective of this, in both cases C_L appears nearly as a single-frequency sinusoid, while the drag coefficient C_D is clearly not. The latter also shows a phase lead relative to C_L. All these outcomes agree very well with simulation results by other authors, for example Gassner et al. [83] or Johnson and

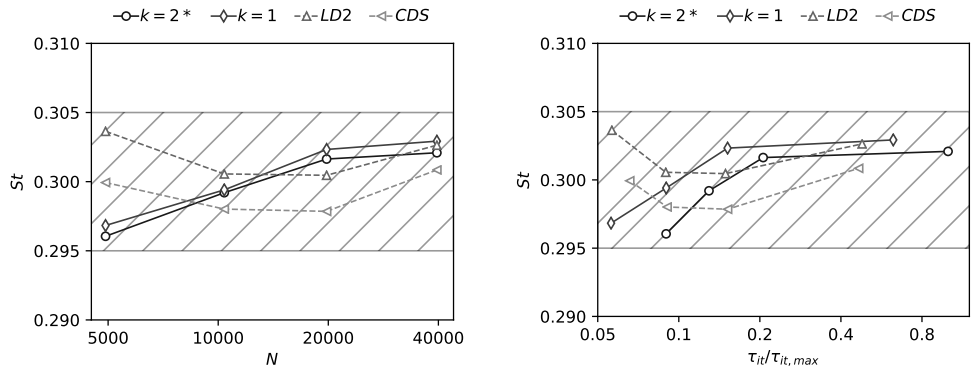

(a) Strouhal number St

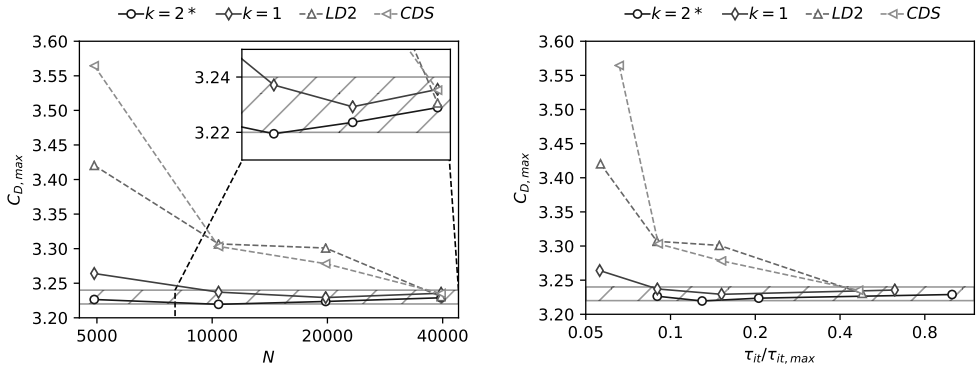

(b) Maximum drag coefficient $C_{D,max}$

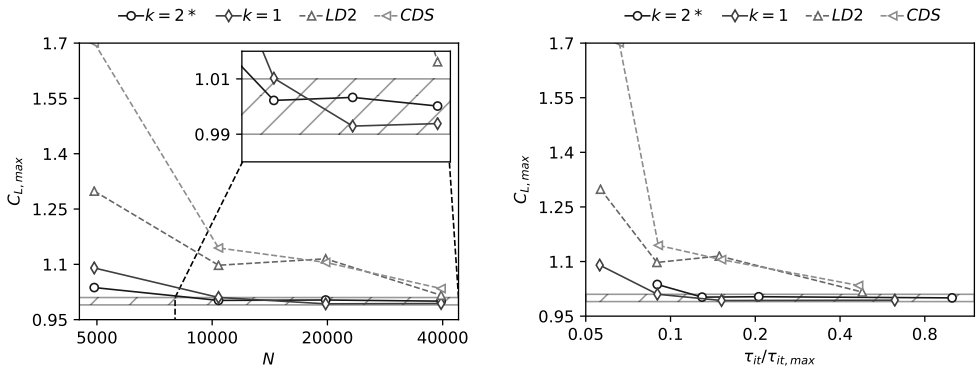

(c) Maximum lift coefficient $C_{L,max}$

Figure 16: Grid convergence study for the laminar flow around a cylinder benchmark in $2D$. Shown are the maximum drag and lift coefficients $C_{D,max}$ and $C_{L,max}$, as well as the Strouhal number St for various meshes with N primary grid nodes (left) and over the normalized average iteration time $\tau_{it}/\tau_{it,max}$. The dashed regions highlight the lower and upper bounds for this benchmark given by Schaefer et al. [81].

Patel [82]. Table 5 lists the force coefficients, the oscillation amplitudes and the Strouhal number that have

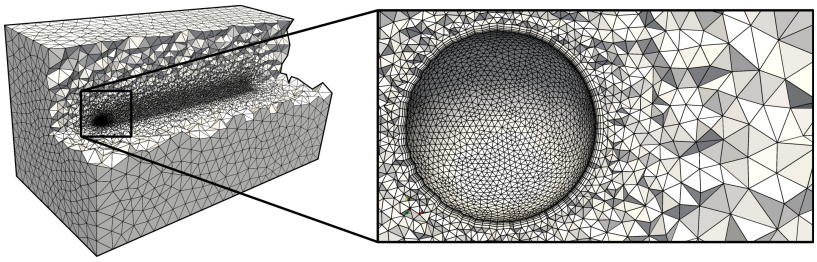

Figure 17: Coarse mesh with $N = 139589$ primary grid nodes used for the simulation of a laminar flow around a sphere in $3D$.

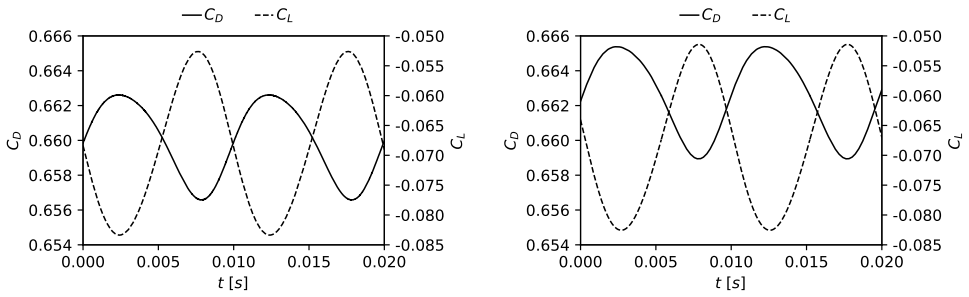

(a) 2*-exact scheme

(b) 1-exact scheme

Figure 18: Temporal evolution of two oscillation periods of the drag coefficient C_D and the lateral force coefficient C_L for the laminar flow around a sphere benchmark, obtained with both k-exact schemes on the finest grid with $N = 610159$.

Table 5: Predicted values for the mean drag coefficient $C_{D,mean}$, the lateral force coefficient $C_{L,mean}$, the respective oscillation amplitudes $C_{D,amp}$ and $C_{L,amp}$ and the Strouhal number St for the laminar flow around a sphere in $3D$. The results have been obtained on the finest mesh with $N = 610159$ nodes and with various discretization schemes.

Reference	$C_{D,mean}$	$C_{L,mean}$	$C_{D,amp}$	$C_{L,amp}$	St
Johnson and Patel [82]	0.656	−0.069	0.0035	0.016	0.137
Gassner et al. [83]	0.673	−0.065	0.0031	0.015	0.135
Kim et al. [84]	0.657	−0.067	–	–	0.134
Tomboulides [85]	0.671	–	0.0031	–	0.137
2*-exact	0.660	−0.068	0.0030	0.015	0.134
1-exact	0.662	−0.067	0.0032	0.016	0.135
$LD2$	0.664	−0.065	0.0029	0.016	0.133
CDS	0.663	−0.069	0.0027	0.015	0.129

been obtained with different discretization schemes on the finest grid. Both k-exact discretization schemes, as well as the $LD2$-scheme, predict all values with only minor deviation compared to reference values given by other authors [82, 83, 84, 85]. Only the CDS-scheme yields larger discrepancies in terms of the Strouhal number St and the amplitude of the drag coefficient $C_{D,amp}$.

The advantage of the k-exact schemes over the conventional discretization methods is even more clear as coarser meshes are employed. Figures 19a-19c shows calculated mean values and amplitudes for the lateral

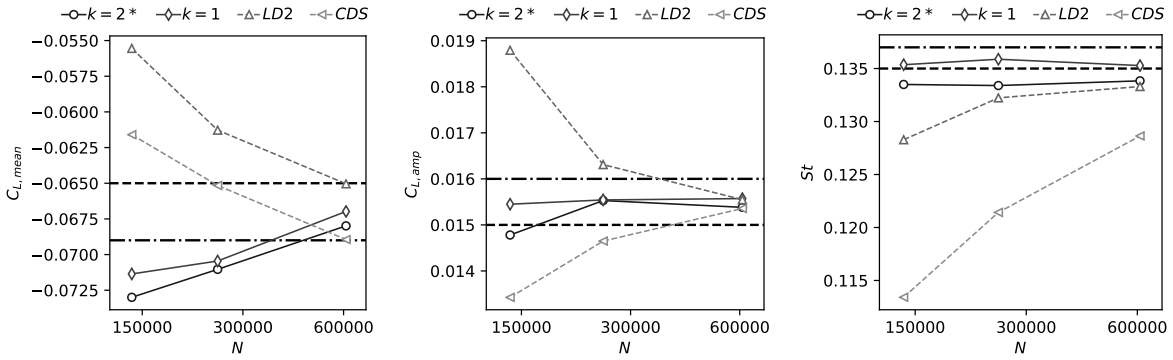

(a) Mean lateral force coefficient $C_{L,mean}$ (b) Lateral force coefficient amplitude $C_{L,amp}$ (c) Strouhal number St

(d) Mean lateral force coefficient $C_{L,mean}$ (e) Lateral force coefficient amplitude $C_{L,amp}$ (f) Strouhal number St

Figure 19: Target indicators for the laminar flow around a sphere benchmark, shown over the number of primary grid nodes N (top), as well as over the normalized average computation time for a single iteration $\tau_{it}/\tau_{it,max}$ (bottom). The dashed dotted lines are reference values given by Johnson and Patel [82] and the straight dashed lines refer to values by Gassner et al [83].

force coefficients for all three grids, as well as the estimated Strouhal number. Straight dashed dotted lines represent reference values by Johnson et al. [82] and the dashed lines are values from Gassner et al. [83]. The latter were estimated with a nodal discontinuous Galerkin scheme with ≈ 3 million degrees of freedom. Both k-exact schemes predict these reference values remarkably well when the grid is coarsened. In contrast to this, the conventional schemes fail to give accurate results especially on the coarsest grid. Figures 19d-19f show the target indicators $C_{L,mean}$, $C_{L,amp}$ and St over the average iteration time τ_{it} normalized by the maximum iteration time obtained in all simulations $\tau_{it,max}$. Compared to the conventional discretization approaches, the mean iteration time increases approximately by a factor of 3.3 if the 2^*-exact schemes is used and by a factor of 1.5 for the 1-exact method. These ratios persist more or less on all three grids. Even though the mean iteration time increases significantly, it can be stated that the overall time to achieve a desired level of accuracy is reduced with the k-exact schemes. This is especially apparent for the 1-exact scheme.

Figure 20 shows three-dimensional vortical structures in the domain which have been identified for the 2^*-exact multiple-correction scheme and both conventional schemes on the finest grid. The structures are

visualized by means of the λ_2-vortex criterion by Jeong and Hussain [86], where a value of $\lambda_2 = -100$ has been chosen to highlight the surfaces. The 1-exact results appear similar to the 2^* solution and thus are not shown for reasons of clarity. It can be observed that the flow preserves a planar symmetry around the plane on which the shedding process is initiated [85]. The shape of these vortical structures also agrees very well with simulation results by several other authors [82, 83, 84, 85, 87]. It should also be noted that the 2^*-exact method is clearly capable of preserving the vortical structures over a long distance. This is also the case for the $LD2$-scheme, even though it features small artifacts in the wake of the sphere. These artifacts are even more apparent for the CDS-scheme, which also gives an inaccurate prediction of the vortex structures further downstream. Figure 21 shows the λ_2-criterion calculated on the coarsest grid. The level of detail is reduced due to larger element sizes. However, compared to both conventional schemes, the 2^*-exact solution still preserves the major flow features with great agreement to the fine case.

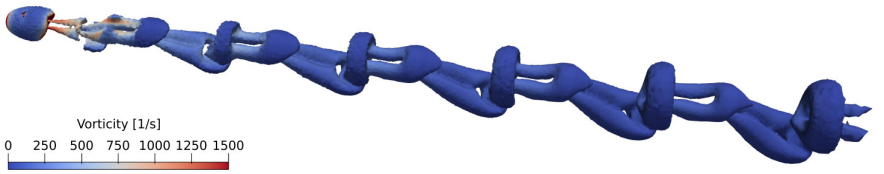

(a) 2^*-exact scheme

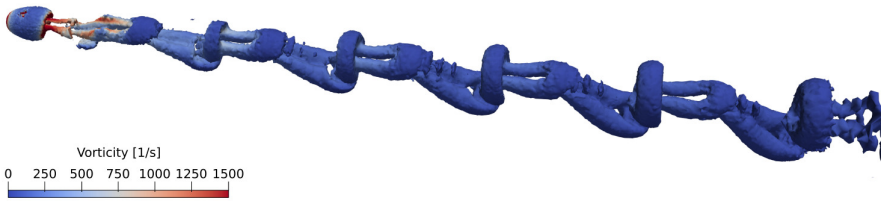

(b) $LD2$ scheme

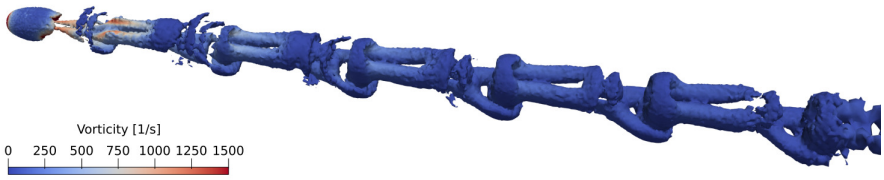

(c) CDS scheme

Figure 20: Vortical structures of the laminar flow around a sphere identified through the λ_2 vortex criterion for $N = 610159$ primary grid nodes.

6. Conclusion

In this work the k-exact multiple-correction method by Pont et al. [13] has been extended to vertex-centered grids. Furthermore, the discretization approach has been incorporated into a fractional step solution strategy for solving the unsteady Navier-Stokes equations. This also involves the implementation of both convective and diffusive fluxes in the k-exact framework, where a single-point integration has been used for the approximation of surface-integrals. The presented method has been implemented in a full-production flow solver by means of a 1- and 2-exact reconstruction and it has been validated by several two- and three-dimensional benchmark problems.

It was shown by means of canonical benchmarks, that the presented approach preserves desired accuracy properties for both convective and diffusive fluxes. Furthermore, the influence on the numerical error was

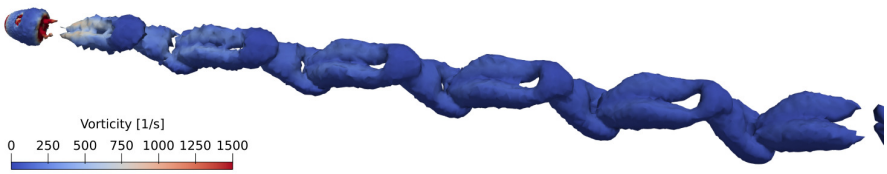

(a) 2^*-exact scheme

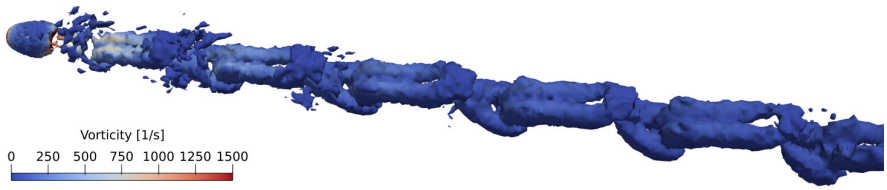

(b) $LD2$ scheme

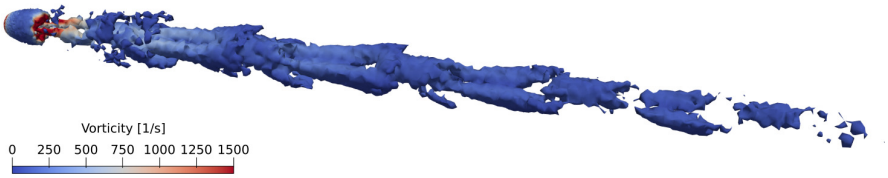

(c) CDS scheme

Figure 21: Vortical structures of the laminar flow around a sphere identified through the λ_2 vortex criterion for $N = 139589$ primary grid nodes.

investigated when using different reconstruction levels for pressure and velocity in the projection method. Compared to a purely 2-exact approach, it was found that the error is only slightly affected when reconstructing the pressure with $k = 1$ and the velocity with $k = 2$. At the same time, the performance of the 2-exact approach could be significantly improved with this configuration. The proposed k-exact approach was also compared to conventional discretization schemes on unstructured grids. It could be demonstrated that our approach clearly enhances the accuracy of simulation results on grids with significantly lower resolution properties, thus leading to an enhanced overall performance. This was also the case for more complicated benchmark simulations, namely the lid driven cavity problem, the laminar flow around a cylinder in $2D$ and the laminar flow around a sphere in $3D$. These benchmarks also showed that the higher accuracy of the presented approach is maintained in the presence of Dirichlet boundary conditions.

For future works, the approach will be used for the simulation of fully turbulent flows on unstructured grids in the framework of large-eddy simulations. Furthermore, the present solution procedure will be extended for the simulation of variable-density low-Mach number flows, so that it can be utilized for combustion applications.

Acknowledgements

This research did not receive any specific grant from funding agencies in the public, commercial, or not-for-profit sectors.

Appendix A. On the calculation of correction matrix $\mathbf{H}_\alpha$

Matrix $\mathbf{H}_\alpha$ is used to obtain a Hessian matrix operator that features an accuracy of $\mathcal{O}(h)$. Its inverse $\mathbf{H}_\alpha^{-1}$ is solely calculated from the mesh geometry. For reasons of clarity, it can be decomposed in two

matrices $\mathbf{A}_\alpha$ and $\mathbf{B}_\alpha$

$$\mathbf{H}_\alpha^{-1} = \frac{1}{2}\left(\mathbf{A}_\alpha + \mathbf{B}_\alpha\right), \tag{A.1}$$

whose entries are calculated according to

$$\mathbf{A}_\alpha = \begin{bmatrix} 2\left.\frac{\partial x_1}{\partial x_1}\right|_{\mathbf{x}_\alpha}^{(0)} & 2\left.\frac{\partial x_2}{\partial x_1}\right|_{\mathbf{x}_\alpha}^{(0)} & 2\left.\frac{\partial x_3}{\partial x_1}\right|_{\mathbf{x}_\alpha}^{(0)} & 0 & 0 & 0 \\ \left.\frac{\partial x_1}{\partial x_2}\right|_{\mathbf{x}_\alpha}^{(0)} & \left.\frac{\partial x_1}{\partial x_1}\right|_{\mathbf{x}_\alpha}^{(0)} + \left.\frac{\partial x_2}{\partial x_2}\right|_{\mathbf{x}_\alpha}^{(0)} & \left.\frac{\partial x_3}{\partial x_2}\right|_{\mathbf{x}_\alpha}^{(0)} & \left.\frac{\partial x_2}{\partial x_1}\right|_{\mathbf{x}_\alpha}^{(0)} & \left.\frac{\partial x_3}{\partial x_1}\right|_{\mathbf{x}_\alpha}^{(0)} & 0 \\ \left.\frac{\partial x_1}{\partial x_3}\right|_{\mathbf{x}_\alpha}^{(0)} & \left.\frac{\partial x_2}{\partial x_3}\right|_{\mathbf{x}_\alpha}^{(0)} & \left.\frac{\partial x_1}{\partial x_1}\right|_{\mathbf{x}_\alpha}^{(0)} + \left.\frac{\partial x_3}{\partial x_3}\right|_{\mathbf{x}_\alpha}^{(0)} & 0 & \left.\frac{\partial x_2}{\partial x_1}\right|_{\mathbf{x}_\alpha}^{(0)} & \left.\frac{\partial x_3}{\partial x_1}\right|_{\mathbf{x}_\alpha}^{(0)} \\ 0 & 2\left.\frac{\partial x_1}{\partial x_2}\right|_{\mathbf{x}_\alpha}^{(0)} & 0 & 2\left.\frac{\partial x_2}{\partial x_2}\right|_{\mathbf{x}_\alpha}^{(0)} & 2\left.\frac{\partial x_3}{\partial x_2}\right|_{\mathbf{x}_\alpha}^{(0)} & 0 \\ 0 & \left.\frac{\partial x_1}{\partial x_3}\right|_{\mathbf{x}_\alpha}^{(0)} & \left.\frac{\partial x_1}{\partial x_2}\right|_{\mathbf{x}_\alpha}^{(0)} & \left.\frac{\partial x_2}{\partial x_3}\right|_{\mathbf{x}_\alpha}^{(0)} & \left.\frac{\partial x_2}{\partial x_2}\right|_{\mathbf{x}_\alpha}^{(0)} + \left.\frac{\partial x_3}{\partial x_3}\right|_{\mathbf{x}_\alpha}^{(0)} & \left.\frac{\partial x_3}{\partial x_2}\right|_{\mathbf{x}_\alpha}^{(0)} \\ 0 & 0 & 2\left.\frac{\partial x_1}{\partial x_3}\right|_{\mathbf{x}_\alpha}^{(0)} & 0 & 2\left.\frac{\partial x_2}{\partial x_3}\right|_{\mathbf{x}_\alpha}^{(0)} & 2\left.\frac{\partial x_3}{\partial x_3}\right|_{\mathbf{x}_\alpha}^{(0)} \end{bmatrix}, \tag{A.2}$$

$$\mathbf{B}_\alpha = \begin{bmatrix} \left.\frac{\partial \mathcal{M}_{11}}{\partial x_1 \partial x_1}\right|_{\mathbf{x}_\alpha}^{(0)} & 2\left.\frac{\partial \mathcal{M}_{12}}{\partial x_1 \partial x_1}\right|_{\mathbf{x}_\alpha}^{(0)} & 2\left.\frac{\partial \mathcal{M}_{13}}{\partial x_1 \partial x_1}\right|_{\mathbf{x}_\alpha}^{(0)} & \left.\frac{\partial \mathcal{M}_{22}}{\partial x_1 \partial x_1}\right|_{\mathbf{x}_\alpha}^{(0)} & 2\left.\frac{\partial \mathcal{M}_{23}}{\partial x_1 \partial x_1}\right|_{\mathbf{x}_\alpha}^{(0)} & \left.\frac{\partial \mathcal{M}_{33}}{\partial x_1 \partial x_1}\right|_{\mathbf{x}_\alpha}^{(0)} \\ \left.\frac{\partial \mathcal{M}_{11}}{\partial x_1 \partial x_2}\right|_{\mathbf{x}_\alpha}^{(0)} & 2\left.\frac{\partial \mathcal{M}_{12}}{\partial x_1 \partial x_2}\right|_{\mathbf{x}_\alpha}^{(0)} & 2\left.\frac{\partial \mathcal{M}_{13}}{\partial x_1 \partial x_2}\right|_{\mathbf{x}_\alpha}^{(0)} & \left.\frac{\partial \mathcal{M}_{22}}{\partial x_1 \partial x_2}\right|_{\mathbf{x}_\alpha}^{(0)} & 2\left.\frac{\partial \mathcal{M}_{23}}{\partial x_1 \partial x_2}\right|_{\mathbf{x}_\alpha}^{(0)} & \left.\frac{\partial \mathcal{M}_{33}}{\partial x_1 \partial x_2}\right|_{\mathbf{x}_\alpha}^{(0)} \\ \vdots & \vdots & \vdots & \cdots & \vdots & \\ \left.\frac{\partial \mathcal{M}_{11}}{\partial x_3 \partial x_3}\right|_{\mathbf{x}_\alpha}^{(0)} & 2\left.\frac{\partial \mathcal{M}_{12}}{\partial x_3 \partial x_3}\right|_{\mathbf{x}_\alpha}^{(0)} & 2\left.\frac{\partial \mathcal{M}_{13}}{\partial x_3 \partial x_3}\right|_{\mathbf{x}_\alpha}^{(0)} & \left.\frac{\partial \mathcal{M}_{22}}{\partial x_3 \partial x_3}\right|_{\mathbf{x}_\alpha}^{(0)} & 2\left.\frac{\partial \mathcal{M}_{23}}{\partial x_3 \partial x_3}\right|_{\mathbf{x}_\alpha}^{(0)} & \left.\frac{\partial \mathcal{M}_{33}}{\partial x_3 \partial x_3}\right|_{\mathbf{x}_\alpha}^{(0)} \end{bmatrix}. \tag{A.3}$$

References

[1] J. A. Ekaterinaris, High-order accurate, low numerical diffusion methods for aerodynamics, Progress in Aerospace Sciences 41 (3-4) (2005) 192–300.

[2] Z. J. Wang, High-order methods for the euler and navier-stokes equations on unstructured grids, Progress in Aerospace Sciences 43 (1-3) (2007) 1–41.

[3] B. Cockburn, C.-W. Shu, Tvb runge-kutta local projection discontinuous galerkin finite element method for conservation laws. ii. general framework, Mathematics of Computation 52 (186) (1989) 411–435.

[4] B. Cockburn, S.-Y. Lin, C.-W. Shu, Tvb runge-kutta local projection discontinuous galerkin finite element method for conservation laws iii: One-dimensional systems, Journal of Computational Physics 84 (1) (1989) 90–113.

[5] B. Cockburn, S. Hou, C.-W. Shu, The runge-kutta local projection discontinuous galerkin finite element method for conservation laws. iv. the multidimensional case, Mathematics of Computation 54 (190) (1990) 545–581.

[6] B. Cockburn, C.-W. Shu, The runge-kutta discontinuous galerkin method for conservation laws v: Multidimensional systems, Journal of Computational Physics 141 (2) (1998) 199–224.

[7] Z. J. Wang, Spectral (finite) volume method for conservation laws on unstructured grids: Basic formulation, Journal of Computational Physics 178 (1) (2002) 210–251.

[8] Z. J. Wang, Y. Liu, D. Kwak, Spectral (finite) volume method for conservation laws on unstructured grids ii: Extension to two dimensional scalar equation, Journal of Computational Physics 179 (2) (2002) 665–697.

[9] Z. J. Wang, Y. Liu, Spectral (finite) volume method for conservation laws on unstructured grids iii: One dimensional systems and partition optimization, Journal of Scientific Computing 20 (1) (2004) 137–157.

[10] Z. J. Wang, L. Zhang, Y. Liu, Spectral (finite) volume method for conservation laws on unstructured grids iv: Extension to two-dimensional systems, Journal of Computational Physics 194 (2) (2004) 716–741.

[11] Y. Liu, M. Vinokur, Z. J. Wang, Spectral difference method for unstructured grids i: Basic formulation, Journal of Computational Physics 216 (2) (2006) 780–801.

[12] Z. J. Wang, Y. Liu, G. May, A. Jameson, Spectral difference method for unstructured grids ii: Extension to the euler equations, Journal of Scientific Computing 32 (1) (2007) 45–71.

[13] G. Pont, D. Puech, P. Brenner, Hybrid rans/les simulation of a space launcher using a high order finite volume scheme and grid intersections technique, in: Symposium on Hybrid RANS-LES Methods, Springer, 2016, pp. 347–356.

[14] T. Barth, P. Frederickson, Higher order solution of the euler equations on unstructured grids using quadratic reconstruction, in: 28th Aerospace Sciences Meeting, 1990, p. 13.
[15] T. J. Barth, Aspects of unstructured grids and finite-volume solvers for the euler and navier-stokes equations, Special Course on Unstructured Grid Methods for Advection Dominated Flows, AGARD Report 787.
[16] C. F. Ollivier-Gooch, Quasi-eno schemes for unstructured meshes based on unlimited data-dependent least-squares reconstruction, Journal of Computational Physics 133 (1) (1997) 6–17.
[17] C. Ollivier-Gooch, M. Van Altena, A high-order-accurate unstructured mesh finite-volume scheme for the advection-diffusion equation, Journal of Computational Physics 181 (2) (2002) 729–752.
[18] A. Nejat, C. Ollivier-Gooch, A high-order accurate unstructured finite volume newton–krylov algorithm for inviscid compressible flows, Journal of Computational Physics 227 (4) (2008) 2582–2609.
[19] C. Ollivier-Gooch, A. Nejat, K. Michalak, Obtaining and verifying high-order unstructured finite volume solutions to the euler equations, AIAA Journal 47 (9) (2009) 2105–2120.
[20] R. Abgrall, On essentially non-oscillatory schemes on unstructured meshes: Analysis and implementation, Journal of Computational Physics 114 (1) (1994) 45–58.
[21] O. Friedrich, Weighted essentially non-oscillatory schemes for the interpolation of mean values on unstructured grids, Journal of Computational Physics 144 (1) (1998) 194–212.
[22] M. Dumbser, M. Käser, Arbitrary high order non-oscillatory finite volume schemes on unstructured meshes for linear hyperbolic systems, Journal of Computational Physics 221 (2) (2007) 693–723.
[23] M. Dumbser, M. Käser, V. A. Titarev, E. F. Toro, Quadrature-free non-oscillatory finite volume schemes on unstructured meshes for nonlinear hyperbolic systems, Journal of Computational Physics 226 (1) (2007) 204–243.
[24] R. Abgrall, A. Larat, M. Ricchiuto, Construction of very high order residual distribution schemes for steady inviscid flow problems on hybrid unstructured meshes, Journal of Computational Physics 230 (11) (2011) 4103–4136.
[25] Compact high order finite volume method on unstructured grids iii: Variational reconstruction, Journal of Computational Physics 337 (2017) 1–26.
[26] Q. Wang, Y.-X. Ren, W. Li, Compact high order finite volume method on unstructured grids i: Basic formulations and one-dimensional schemes, Journal of Computational Physics 314 (2016) 863–882.
[27] F. Haider, P. Brenner, B. Courbet, J.-P. Croisille, Parallel implementation of k-exact finite volume reconstruction on unstructured grids, in: High Order Nonlinear Numerical Schemes for Evolutionary PDEs, Springer, 2014, pp. 59–75.
[28] F. Haider, Discrétisation en maillage non structuré général et applications les, Ph.D. thesis, Université Pierre et Marie Curie-Paris VI (2009).
[29] F. Haider, P. Brenner, B. Courbet, J. P. Croisille, Efficient implementation of high order reconstruction in finite volume methods, Finite Volumes for Complex Applications VI - Problems and Perspectives, Springer Proceedings in Mathematics 4 (2011) 553–560.
[30] F. Haider, N. Bertier, B. Courbet, F. Vuillot, J. Croisille, Application of a High Order Finite Volume Scheme on Unstructured Grids to Fluid Dynamics and Aerothermochemistry, hal-01111360 (Jan. 2015).
URL https://hal.archives-ouvertes.fr/hal-01111360
[31] Q. Wang, Y.-X. Ren, W. Li, Compact high order finite volume method on unstructured grids ii: Extension to two-dimensional euler equations, Journal of Computational Physics 314 (2016) 883–908.
[32] Y.-S. Zhang, Y.-X. Ren, Q. Wang, Compact high order finite volume method on unstructured grids iv: Explicit multi-step reconstruction schemes on compact stencil, Journal of Computational Physics 396 (2019) 161–192.
[33] G. Pont, P. Brenner, P. Cinnella, B. Maugars, J.-C. Robinet, Multiple-correction hybrid k-exact schemes for high-order compressible rans-les simulations on fully unstructured grids, Journal of Computational Physics 350 (2017) 45–83.
[34] G. Pont, Self adaptive turbulence models for unsteady compressible flows, Ph.D. thesis, Ecole Nationale Supérieure d'Arts et Métiers-ENSAM (2015).
[35] A. Menasria, P. Brenner, P. Cinnella, G. Pont, Toward an improved wall treatment for multiple-correction k-exact schemes, in: 2018 Fluid Dynamics Conference, 2018, p. 4164.
[36] M. Bernard, G. Lartigue, G. Balarac, V. Moureau, G. Puigt, A framework to perform high-order deconvolution for finite-volume method on simplicial meshes, International Journal for Numerical Methods in Fluids.
[37] F. Bassi, A. Crivellini, D. A. Di Pietro, S. Rebay, An implicit high-order discontinuous galerkin method for steady and unsteady incompressible flows, Computers & Fluids 36 (10) (2007) 1529–1546.
[38] A. J. Chorin, Numerical solution of the navier-stokes equations, Mathematics of computation 22 (104) (1968) 745–762.
[39] J.-L. Guermond, P. Minev, J. Shen, An overview of projection methods for incompressible flows, Computer Methods in Applied Mechanics and Engineering 195 (44-47) (2006) 6011–6045.
[40] L. Quartapelle, Numerical Solution of the Incompressible Navier-Stokes Equations, Vol. 113, International Series of Numerical Mathematics, Birkhäuser, 2013.
[41] J. H. Ferziger, M. Perić, R. L. Street, Computational Methods for Fluid Dynamics, Vol. 3, Springer, 2002.
[42] J.-M. Lourier, A. Huber, B. Noll, M. Aigner, Numerical analysis of indirect combustion noise generation within a subsonic nozzle, AIAA Journal 52 (10) (2014) 2114–2126.
[43] A. Fiolitakis, P. R. Ess, P. Gerlinger, M. Aigner, Modeling of heat transfer and differential diffusion in transported pdf methods, Combustion and Flame 161 (8) (2014) 2107–2119.
[44] J.-M. Lourier, M. Stöhr, B. Noll, S. Werner, A. Fiolitakis, Scale adaptive simulation of a thermoacoustic instability in a partially premixed lean swirl combustor, Combustion and Flame 183 (2017) 343–357.
[45] C. Eberle, P. Gerlinger, K. P. Geigle, M. Aigner, Toward finite-rate chemistry large-eddy simulations of sooting swirl flames, Combustion Science and Technology 190 (7) (2018) 1194–1217.
[46] G. Eckel, P. Le Clercq, T. Kathrotia, A. Saenger, S. Fleck, M. Mancini, T. Kolb, M. Aigner, Entrained flow gasification.

part 3: Insight into the injector near-field by large eddy simulation with detailed chemistry, Fuel 223 (2018) 164–178.
[47] G. Eckel, J. Grohmann, L. Cantu, N. Slavinskaya, T. Kathrotia, M. Rachner, P. Le Clercq, W. Meier, M. Aigner, Les of a swirl-stabilized kerosene spray flame with a multi-component vaporization model and detailed chemistry, Combustion and Flame 207 (2019) 134–152.
[48] M. Grader, C. Eberle, P. Gerlinger, Large-eddy simulation and analysis of a sooting lifted turbulent jet flame, Combustion and Flame 215 (2020) 458–470.
[49] B. Enderle, B. Rauch, F. Grimm, G. Eckel, M. Aigner, Non-intrusive uncertainty quantification in the simulation of turbulent spray combustion using polynomial chaos expansion: A case study, Combustion and Flame 213 (2020) 26–38.
[50] J. Blazek, Computational Fluid Dynamics: Principles and Applications, Butterworth-Heinemann, 2015.
[51] B. Diskin, J. L. Thomas, E. J. Nielsen, H. Nishikawa, J. A. White, Comparison of node-centered and cell-centered unstructured finite-volume discretizations: Viscous fluxes, AIAA Journal 48 (7) (2010) 1326–1338.
[52] H. Nishikawa, Beyond interface gradient: A general principle for constructing diffusion schemes, in: 40th Fluid Dynamics Conference and Exhibit, 2010, p. 5093.
[53] H. Nishikawa, Uses of zero and negative volume elements for node-centered edge-based discretization, in: 23rd AIAA Computational Fluid Dynamics Conference, 2017, p. 4295.
[54] H. Nishikawa, A face-area-weighted centroid formula for reducing grid skewness and improving convergence of edge-based solver on highly-skewed simplex grids, in: AIAA Scitech 2020 Forum, 2020, p. 1786.
[55] H. Nishikawa, A face-area-weighted 'centroid' formula for finite-volume method that improves skewness and convergence on triangular grids, Journal of Computational Physics 401 (2020) 109001.
[56] J. M. Pozo, M.-C. Villa-Uriol, A. F. Frangi, Efficient 3d geometric and zernike moments computation from unstructured surface meshes, IEEE Transactions on Pattern Analysis and Machine Intelligence 33 (3) (2011) 471–484.
[57] P. Koehl, Fast recursive computation of 3d geometric moments from surface meshes, IEEE Transactions on Pattern Analysis and Machine Intelligence 34 (11) (2012) 2158–2163.
[58] M. R. Charest, T. R. Canfield, N. R. Morgan, J. Waltz, J. G. Wohlbier, A high-order vertex-based central eno finite-volume scheme for three-dimensional compressible flows, Computers & Fluids 114 (2015) 172–192.
[59] J. L. Thomas, B. Diskin, H. Nishikawa, A critical study of agglomerated multigrid methods for diffusion on highly-stretched grids, Computers & Fluids 41 (1) (2011) 82–93.
[60] W. Li, Y.-X. Ren, High-order k-exact weno finite volume schemes for solving gas dynamic euler equations on unstructured grids, International Journal for Numerical Methods in Fluids 70 (6) (2012) 742–763.
[61] M. R. Charest, C. P. Groth, P. Q. Gauthier, A high-order central eno finite-volume scheme for three-dimensional low-speed viscous flows on unstructured mesh, Communications in Computational Physics 17 (3) (2015) 615–656.
[62] F. Setzwein, P. Ess, P. Gerlinger, High-order k-exact finite volume scheme for vertex-centered unstructured grids, in: AIAA Scitech 2020 Forum, 2020, p. 1785.
[63] F. Setzwein, M. Spraul, P. Ess, P. Gerlinger, On the structure of correction matrices for a k-exact high-order finite-volume scheme on vertex-centered unstructured grids, in: AIAA Scitech 2021 Forum, 2021, p. 1548.
[64] I. Mary, P. Sagaut, Large eddy simulation of flow around an airfoil near stall, AIAA journal 40 (6) (2002) 1139–1145.
[65] N. Tajallipour, B. B. Owlam, M. Paraschivoiu, Self-adaptive upwinding for large eddy simulation of turbulent flows on unstructured elements, Journal of aircraft 46 (3) (2009) 915–926.
[66] J. Löwe, A. Probst, T. Knopp, R. Kessler, Low-dissipation low-dispersion second-order scheme for instructured finite volume flow solvers, AIAA Journal (2016) 2961–2971.
[67] S. Mathur, J. Murthy, A pressure-based method for unstructured meshes, Numerical Heat Transfer 31 (2) (1997) 195–215.
[68] H. Nishikawa, A hyperbolic poisson solver for tetrahedral grids, Journal of Computational Physics (2020) 109358.
[69] B. Diskin, J. L. Thomas, Comparison of node-centered and cell-centered unstructured finite-volume discretizations: Inviscid fluxes, AIAA Journal 49 (4) (2011) 836–854.
[70] R. Temam, Sur l'approximation de la solution des équations de navier-stokes par la méthode des pas fractionnaires (ii), Archive for Rational Mechanics and Analysis 33 (5) (1969) 377–385.
[71] C. Rhie, W. L. Chow, Numerical study of the turbulent flow past an airfoil with trailing edge separation, AIAA Journal 21 (11) (1983) 1525–1532.
[72] H. K. Versteeg, W. Malalasekera, An Introduction to Computational Fluid Dynamics: The Finite Volume Method, Pearson Education, 2007.
[73] A. Probst, J. Löwe, S. Reuß, T. Knopp, R. Kessler, Scale-resolving simulations with a low-dissipation low-dispersion second-order scheme for unstructured flow solvers, AIAA Journal 54 (10) (2016) 2972–2987.
[74] P. Khosla, S. Rubin, A diagonally dominant second-order accurate implicit scheme, Computers & Fluids 2 (2) (1974) 207–209.
[75] T. Knopp, X. Zhang, R. Kessler, G. Lube, Enhancement of an industrial finite-volume code for large-eddy-type simulation of incompressible high reynolds number flow using near-wall modelling, Computer Methods in Applied Mechanics and Engineering 199 (13-16) (2010) 890–902.
[76] O. Botella, R. Peyret, Benchmark spectral results on the lid-driven cavity flow, Computers & Fluids 27 (4) (1998) 421–433.
[77] C.-H. Bruneau, M. Saad, The 2d lid-driven cavity problem revisited, Computers & fluids 35 (3) (2006) 326–348.
[78] U. Ghia, K. N. Ghia, C. Shin, High-re solutions for incompressible flow using the navier-stokes equations and a multigrid method, Journal of Computational Physics 48 (3) (1982) 387–411.
[79] S. Tu, S. Aliabadi, Development of a hybrid finite volume/element solver for incompressible flows, International Journal for Numerical Methods in Fluids 55 (2) (2007) 177–203.
[80] B. Xie, S. Ii, A. Ikebata, F. Xiao, A multi-moment finite volume method for incompressible navier-stokes equations on unstructured grids: Volume-average/point-value formulation, Journal of Computational Physics 277 (2014) 138–162.

[81] M. Schäfer, S. Turek, F. Durst, E. Krause, R. Rannacher, Benchmark computations of laminar flow around a cylinder, in: Flow Simulation with High-Performance Computers II, Springer, 1996, pp. 547–566.
[82] T. Johnson, V. Patel, Flow past a sphere up to a reynolds number of 300, Journal of Fluid Mechanics 378 (1999) 19–70.
[83] G. J. Gassner, F. Lörcher, C.-D. Munz, J. S. Hesthaven, Polymorphic nodal elements and their application in discontinuous galerkin methods, Journal of Computational Physics 228 (5) (2009) 1573–1590.
[84] J. Kim, D. Kim, H. Choi, An immersed-boundary finite-volume method for simulations of flow in complex geometries, Journal of Computational Physics 171 (1) (2001) 132–150.
[85] A. Tomboulides, S. Orszag, G. Karniadakis, Direct and large-eddy simulations of axisymmetric wakes, in: 31st Aerospace Sciences Meeting, 1993, p. 546.
[86] J. Jeong, F. Hussain, On the identification of a vortex, Journal of Fluid Mechanics 285 (1995) 69–94.
[87] T. Haga, H. Gao, Z. J. Wang, A high-order unifying discontinuous formulation for the navier-stokes equations on 3d mixed grids, Mathematical Modelling of Natural Phenomena 6 (3) (2011) 28–56.